Revision 3

Word count: 15249

Magmatic degassing and fluid metasomatism promote compositional variation from I-type to peralkaline A-type granite in late Cretaceous Fuzhou felsic complex, SE China

Feng Zhang[1, 2, 3], Feng Guo[1, 2*], Xiaobing Zhang[1, 2], Liang Zhao[1, 2]

1 State Key Laboratory of Isotope Geochemistry, Guangzhou Institute of Geochemistry, Chinese Academy of Sciences, Guangzhou 510640, China

2 Chinese Academy of Sciences Center for Excellence in Deep Earth Science, Guangzhou 510640, China

3 College of Earth and Planetary Sciences, University of Chinese Academy of Sciences, Beijing 10100049, China

**** Corresponding author, email: guofengt@263.net.***

15 # Abstract

16 A-type granites generally have much lower water but higher temperature and
17 incompatible element concentrations than I-type granitoids. Yet it remains unclear
18 why I-A-type granitic complexes occur in convergent plate margins. Here we conduct
19 geochemical analyses on apatite and mafic minerals from the late Cretaceous I-A-type
20 granitic complex in Fuzhou area, SE China, aiming to decipher differentiation, fluid
21 metasomatism and degassing that primarily control the compositional diversity of
22 felsic magmas. Apatites in both rock types are F-rich and show large H_2O and δD
23 variations, i.e., 341 − 3892 ppm H_2O and −325 − +336‰ δD in I-type granitoids;
24 67−1366 ppm H_2O and −251 − +1439‰ δD in A-type granites. H_2O in apatite is
25 negatively correlated with La/Sm and Sr/Y in the I-type granitoids, whereas it is
26 positively correlated with Ce and total rare earth element (REE) concentrations in the
27 A-type granites. Once H_2O decreases up to hundreds of ppm, both rock types show a
28 rapid decrease of H_2O/Ce, an increase of F/Cl and extensive H isotope fractionation.
29 Arfvedsonite occurs as a late crystallizing mineral in the A-type granite and has
30 much higher contents of Na_2O, K_2O, F and high field strength elements (HFSE) than
31 hornblende in the I-type granitoids, indicating addition of F-HFSE-rich alkaline fluids
32 during its magmatic evolution. The consumption of arfvedsonite and formation of
33 aegirine further indicate the role of fluid metasomatism and H_2 degassing via a
34 reaction of $3Na_3Fe_5Si_8O_{22}(OH)_2 + 2H_2O = 9NaFeSi_2O_6 + 2Fe_3O_4 + 6SiO_2+5H_2$.
35 The combined geochemical data demonstrate that the systematic differences in
36 mineral assemblage, whole-rock composition, magma temperature, H_2O and δD of

apatite between the I-type and A-type granites are likely attributed to varying degrees of differentiation, fluid metasomatism and magmatic degassing. The I-type granitoids experienced hornblende, biotite, plagioclase, K-feldspar and apatite fractionation and close-system degassing. The A-type granite was likely formed from the I-type monzogranitic magma that was metasomatized by the mantle-derived F-HFSE-rich alkaline fluids to produce the peralkaline magma, which further experienced K-feldspar + plagioclase + biotite + apatite fractionation and open-system degassing. Further numerical estimation indicates that the primary magma of Fuzhou granitic complex contained ~3.0 wt% H_2O and the lower water content of A-type granite was likely attributed to strong degassing during its emplacement. Our results indicate that some peralkaline A-type granites can be generated from relatively water-poor I-type granitic magmas by fluid metasomatism and degassing.

Keywords: Magmatic degassing; Fluid metasomatism; Water content and H isotopes; Apatite; Fuzhou I-A-type granitic complex; SE China

52 # Introduction

53 Granite represents the most important component distinguishing the Earth from
54 the other planets in the solar system. Based on geochemistry and tectonic setting,
55 granites can be subdivided into I-, A-, S- and M-types (Whalen et al., 1987; Eby,
56 1990). It has widely been recognized that A-type granites are characterized by
57 hypersolvus to subsolvus texture of alkali feldspar and contain characteristic minerals
58 such as arfvedsonite and aegirine, indicative of alkaline to peralkaline affinity of the
59 parent magmas (e.g., Bonin, 2007; Collins et al., 1982; Salvi and Williams-Jones,
60 2006). Also, A-type granites commonly have much lower water contents but higher
61 concentrations of most incompatible elements [e.g., K, Rb, Nb, Zr, Y and rare earth
62 elements (REEs)], F and higher magma temperatures than I-type granitoids (Collins et
63 al., 1982; Bonin, 2007).

64 Previous experiments suggested that A-type granites could contain 2.4−4.3 wt%
65 H_2O (Clemens et al., 1986; Patiño Douce, 1997). On the basis of phase equilibrium,
66 Creaser and White (1991) proposed that the A-type volcanic rocks in southern
67 Australia contained 1−2 wt% H_2O. Based on experimental data, Huang et al. (2019)
68 suggested that A-type granites even contained 6.5−8.0 wt% H_2O. In contrast, Wei et al.
69 (2000) reported that the H_2O contents were around 0.1 wt% for the late Cretaceous
70 peralkaline A-type granites in eastern China, with a δD value from −145 to −99‰.
71 Compared to A-type granites, I-type granitoids usually contain abundant hornblende,
72 which is a water-bearing mineral and crystallizes in a H_2O-rich system (H_2O > 4wt%,
73 e.g., Dall'Agnol et al., 1999; Holtz et al., 2001; Thomas and Davidson, 2012).

Nevertheless, O'Neil and Chappell (1977) reported that the I-type granitoid magmas in the New England batholith contained 0.23−0.69 wt% H_2O with a δD value from −102 to −52‰. Collectively, it remains unclear about the H_2O contents of primary magmas respectively for I-type and A-type granites.

Tectonically, A-type granites generally occur in intraplate setting (e.g., continental rift, plume and hotspot), while I-type granitoids usually form at convergent plate margins (e.g., Pitcher, 1997; Bonin, 2007; Collins et al., 2019; Condie et al., 2023). However, I-A granitic complexes have widely been identified in active continental margins and orogenic belts, such as the Lachlan orogenic belt (Turner et al., 1992; Chappell and White, 1992), the Central Asian orogenic belt (e.g., Geng et al., 2009; Tang et al., 2010, 2012), the Southeast (SE) China (e.g., the Zhangpu and Zhangzhou plutons) (Chen et al., 2013, 2022; Zhao et al., 2016) and the Gangdese belt (Hao et al., 2019). Petrogenetic models of the I-A granitic complexes include: (1) the earlier I-type granitoids originate from melting of a metaigneous source, and the later A-type granites are formed by melting of volatile-rich (such as F or Cl) granulitic residue at higher temperature (Landenberger and Collins, 1996); (2) I-type granitoids are produced by melting of metaigneous rocks at the lower crust, and the associated A-type granites represent melts of the early I-type granitoids (e.g., Farahat et al., 2007); (3) Both I-type and A-type granites are cogenetic with more involvement of a mantle-derived component in the A-type granite (e.g., Kerr and Fryer, 1993; Chen et al., 2022); (4) I-type and A-type granites are petrogenetically unrelated through melting of different crustal protoliths, with the formation of A-type

96 granite related to metasomatism of F-HFSE-rich alkaline fluid released from
97 mantle-derived alkaline magma (e.g., Montero et al., 2009).

98 These previous hypotheses have primarily been focused on the protoliths and
99 melting process to interpret the compositional differences between I- and A-type
100 granites. Yet, it remains unclear why A-type granite is H_2O-poor relative to its I-type
101 counterpart. Possible reasons include H_2O concentration differences of the source
102 protoliths, varying degrees of magmatic differentiation and degassing. In particular,
103 the influence of volatiles on the evolution of magma may have been neglected in the
104 previous literature.

105 Apatite ($Ca_5[PO_4]_3[F, Cl, OH]$), as a ubiquitous accessory mineral in various
106 igneous rocks (e.g., Sha and Chappell.,1999; Pan and Fleet, 2002; Bruand et al., 2017),
107 can incorporate volatiles, major and trace elements of various geochemical behaviors
108 into its lattice (e.g., F, Cl, OH, S, Sr, Y and REE) (e.g., Bruand et al., 2014; Harlov,
109 2015). Apatite geochemistry is useful to track magma petrogenesis with compositional
110 ranges from mafic to felsic (Chu et al., 2009; Teiber et al., 2014; Ladenburger et al.,
111 2016; Stock et al, 2018, Zhang et al., 2020, 2021; Sun et al., 2022),
112 magmatic-hydrothermal processes (Zeng et al., 2016b; Zhang et al., 2020; Cao et al.,
113 2021), and mineralization (e.g., Mao et al., 2016; Xiao et al., 2021). Up to now, the H,
114 O, Cl and Nd isotope compositions and H_2O content in apatite have widely been
115 applied to understand the evolution of Earth and other planets (e.g., Kusebauch et al.
116 2015; Andersson et al., 2019; Bruand et al., 2019; Hu et al., 2020, 2021).

117 In this contribution, we perform geochemical analyses (including microtexture,

major and trace element compositions, H_2O and H isotope compositions) on apatite and mafic minerals from the I-A-type granitic complex in Fuzhou area, SE China, together with additional whole-rock geochemical analyses, aiming to: (1) discuss the roles of magmatic differentiation, fluid metasomatism and devolatilization in producing the geochemical variation from I-type to peralkaline A-type granitoids in the Fuzhou complex; and (2) estimate the H_2O contents of parental magma of different granitic rock types; and (3) propose a comprehensive model to illustrate the petrogenetic relationships between the I-type and A-type granitoids.

Geological Backgrounds and Sample descriptions

Geological setting

The South China Block consists of the Yangtze block in its northwest and the Cathaysia block in its southeast, which were amalgamated in the Neoproterozoic along the Jiangnan Orogenic Belt (Fig. 1; Li et al., 2009; Zhang et al. 2013). It underwent extensive tectonic and magmatic activity related to the advancing subduction and rollback of paleo-Pacific slab during Mesozoic (e.g., Zhou and Li, 2000; Wang et al., 2013; Guo et al., 2021). The distribution of Mesozoic igneous rocks in SE China is mainly controlled by several large-scale NE-trending faults like the Zhenghe-Dafu and Changle-Nan'ao faults (Fig. 1). The magmatism consists of predominant felsic rocks with minor mafic rocks (Zhou et al., 2006; Guo et al., 2012; Zhao et al., 2021). The mafic igneous rocks generally show hybrid geochemical signatures, reflecting complex crust-mantle interaction at subduction zones (e.g., Xu

et al., 1999; Griffin et al., 2002; Zhang et al., 2019). The felsic intrusive rocks exposed in this region are mainly shallow-level, calc-alkaline, I-type granitoids, spanning a wide rock spectrum from diorite, granodiorite to monzogranite (e.g., Zhou et al. 2006; Chen et al., 2013), with some peralkaline granites (or A-type granites) emplaced during late Cretaceous (e.g., Martin et al., 1994; Qiu et al., 1999; Zhao et al., 2016). In the areas such as Fuzhou, Zhangpu and Zhangzhou, coeval I- and A-type granitoids constitute I-A-type granitic complexes (Martin et al., 1994; Zhao et al., 2016; Chen et al., 2019b, 2022).

Sample description

The Fuzhou I-A-type granitic complex consists of the Danyang, Fuzhou, Kuiqi, and Bijiashan plutons (Fig. 1c). The field geology, lithological assemblage, mineral composition and age information are summarized below.

The Danyang pluton constitutes the northern part of the complex that intrudes into the early Cretaceous Nanyuan Fm. felsic lavas (J_3n). It consists of coarse- to medium-grained monzonite, granodiorite and monzogranite, constituting an I-type lithological assemblage from intermediate to felsic composition (e.g., Martin et al., 1994). The major minerals in the monzonite include hornblende (8%) + biotite (15%) + plagioclase (60%, $An_{40\sim54}$) + quartz (10%) +K-feldspar (5%) and accessary minerals such as apatite, zircon, allanite and Fe-Ti oxides (Fig. 2a and b). The mineral assemblage of granodiorite is hornblende (3%) + biotite (10%) + plagioclase (50%, $An_{30\sim50}$) + K-feldspar (15%) + quartz (20%), with accessary minerals like ilmenite,

160 sphene, zircon, apatite and allanite (Fig. 2c and d). Monzogranite is composed of
161 plagioclase (30%, An_{40}) + K-feldspar (30%) + quartz (30%) + biotite (8%) +
162 hornblende (2%), with accessory minerals like zircon, apatite and ilmenite (Fig. 2e
163 and f). Previous whole-rock Rb-Sr dating results indicated the emplacement of
164 Danyang monzogranite at 103±10 Ma (Huang et al., 1986; Martin et al., 1994). Lin et
165 al. (2011) also proposed that the Danyang monzogranite was formed during 96−106
166 Ma (±5 Ma) based on zircon U-Pb ages analyzed by laser ablation-inductively
167 coupled plasma-mass spectrometer (LA-ICP-MS). In addition, Chen et al. (2019a)
168 used a secondary ion mass spectrometer (SIMS, ims-1280) to analyze the zircons
169 from the Danyang monzogranite and diorite (they also named it as Nanyu pluton),
170 yielding younger zircon U-Pb ages of 97−99 Ma (±1 Ma).

171 The Fuzhou pluton represents the southwestern part of the complex. It generally
172 comprises grey coarse-grained monzogranite (e.g., Martin et al., 1994), with a mineral
173 assemblage of plagioclase (20−30%, An_{25}), alkali feldspar (30−40%, $An_{\sim 40}$), quartz
174 (30%), biotite (5%), hornblende (2%) as well as accessory minerals like ilmenite,
175 zircon and apatite (Figs. 2e, f and S1a, b). Zhu et al. (2021) reported a LA-ICP-MS
176 zircon U-Pb age of 106 ± 0.8 Ma, similar to a whole-rock Rb-Sr isochron age of 104 ±
177 5 Ma by Martin et al. (1994). This age is apparently older than the SIMS zircon U-Pb
178 age of 97±1 Ma (Chen et al., 2019b).

179 The Kuiqi pluton is the southern part of the complex with an area about 300 km^2.
180 It consists of grey-pink peralkaline granite (e.g., Martin et al., 1994). There are clear
181 contact relationships among the Kuiqi, Danyang and Fuzhou plutons (Fig. 1).

182 According to Martin et al. (1994), the Kuiqi pluton intrudes into calc-alkaline I-type
183 granitoids. The mineral assemblage includes alkali feldspar (45−55%) + plagioclase
184 (10−20%) + quartz (30%) + arfvedsonite (2%) + aegirine (1%), with accessory
185 minerals like zircon, ilmenite and apatite (Figs. 2g, h and S1c-f). The occurrence of
186 apatite is rare in the peralkaline granite. Arfvedsonite is xenomorphic and occurs as
187 interstitial crystal in association with aegirine, indicating its crystallization during the
188 late stage of magmatic evolution (Fig. 2g). Fluorite occasionally occurs as inclusion in
189 arfvedsonite. Miarolitic texture is generally present at the margins of the intrusion
190 (e.g., 19KQ01-07 and 21KQ20-22), filled with K-feldspar, quartz, fluorite,
191 arfvedsonite and aegirine. The emplacement of Kuiqi peralkaline granite have well
192 been dated by LA-ICP-MS and SIMS zircon U-Pb ages and whole-rock Rb-Sr
193 isochrons, yielding an age range from 93 to 97 Ma with analytical errors ±1 Ma for
194 the SIMS method (Chen et al., 2019b; Martin et al., 1994; Zhu et al., 2021; Zeng et al.,
195 2016).

196 Although the previous dating results by different methods suggest the
197 emplacement of Fuzhou I-A granitic complex during the time period of 106-93 Ma,
198 the SIMS zircon U-Pb dating results of Danyang, Fuzhou and Kuiqi plutons yield a
199 similar age between 96~99 Ma (Chen et al., 2019a, b). Contact relationships suggest
200 that the A-type granites are slightly younger than the I-type granitoids (Martin et al.,
201 1994). The combined observations from spatial contact relationships, systematic
202 variation in mineral assemblage and similar age information indicate that these three
203 plutons constitute a late Cretaceous I-A-type granitic complex. The formation of

Fuzhou complex is consistent with an extensional setting probably as a result of rollback and tearing of the subducting paleo-Pacific slab (e.g., Guo et al., 2021).

In this study, ten samples of I-type granitoids were collected from the Danyang (19DY01-11) and Fuzhou (19FZ07-09 and 19JX01-04) plutons, and the other eleven samples of A-type granites were gathered from the Kuiqi pluton (19KQ01-06 and 21KQ02-22).

Analytical methods

Whole-rock geochemical analyses

The major element compositions of whole-rock samples were measured by a wavelength X-ray fluorescence spectrometry (XRF) at the State Key Laboratory of Isotope Geochemistry, Guangzhou Institute of Geochemistry (GIG), Chinese Academy of Sciences (CAS). About 0.5g of powder was mixed with 3.6 g $Li_2B_4O_7$, 0.4g LiF, 0.3g NH_4NO_3, and minor LiBr in a platinum crucible (Zhang et al., 2020). It was then fused in a furnace to make a glass disk for major oxide analysis. Trace element contents were performed on a Perkin-Elmer ELAN 6000 inductively coupled plasma mass spectrometry (ICP-MS) at the GIG, CAS. About 50 mg sample powder was mixed with 1 mL HF and 0.5 mL HNO_3 in a Teflon beaker, which was then sealed in a stainless-steel bomb and heated at 190 °C for two days. Detailed analytical procedure was reported in Liu et al. (1996). The analytical errors were ~5% for rare earth element (REE) and were 5 to ~10% for high field strength element (HFSE) and other trace elements, estimated from repetitive analyses of USGS standards GSR-1

(granite), GSR-2 (andesite) and GSR-3 (basalt).

Whole-rock Nd isotope analyses were conducted in a Finnigan Neptune multi-collector ICP-MS at the GIG, CAS, following the analytical procedures in Li et al. (2006). Cation columns were used to separate REE, and Nd fraction was then separated by a HDEHP-coated Kef column. The blank of the analytical procedure was about 30 pg for Nd. The measured $^{143}Nd/^{144}Nd$ ratios were normalized to $^{146}Nd/^{144}Nd$ = 0.7219 (Li et al., 2006). The analyzed $^{143}Nd/^{144}Nd$ ratios were adjusted to the standards of the JNdi-1 ($^{143}Nd/^{144}Nd$= 0.512115 ± 4, 2σ, n=4). During the analyses, the USGS reference BHVO-2 (basalt) gave $^{143}Nd/^{144}Nd$ = 0.512980 ± 6 (2σ, n = 4), in agreement with the recommended isotope ratios by Weis et al. (2005). The $\varepsilon_{Nd}(t)$ is calculated by the equation: $\varepsilon_{Nd}(t) = \{[^{143}Nd/^{144}Nd - ^{147}Sm/^{144}Nd \times (e^{\lambda t}-1)] / [(^{143}Nd/^{144}Nd)_{CHUR}(0) - (^{147}Sm/^{144}Nd)_{CHUR}] \times (e^{\lambda t}-1)] - 1\} \times 10^4$, where λ = 6. 54 × 10^{-12} year $^{-1}$ (Lugmair and Marti, 1977), $(^{143}Nd/^{144}Nd)_{CHUR}(0)$ = 0.512638 and $(^{147}Sm/^{144}Nd)_{CHUR}$ = 0.1967 (Bouvier et al. 2008). The whole-rock major and trace element and Nd isotopic compositions are listed in Table S1.

In-situ compositional analyses on minerals

The apatite crystals were mounted in epoxy and further polished to show their internal texture. All microscopic images and *in-situ* geochemical analyses on apatite and mafic minerals were carried out at the GIG, CAS. The detailed description was reported in He et al. (2020). The BSE images of apatite were taken with a Carl Zeiss SUPRA 55 SAPPHIRE Field Emission-Scanning Electron Microscope (SEM). X-ray

intensity mapping of apatite was performed on electron probe microanalysis (EPMA) using a Cameca SX FiveFe instrument with operating conditions of 15 kV accelerating voltage and 50 nA beam current with focused spots ranging from 0.1 to 0.2 μm. The respective detection limits of the instrument for F, Cl, Na, Ce, and S are 800 ppm, 200 ppm, 70 ppm, 400 ppm, and 50 ppm.

The major element concentrations in apatite, hornblende, arfvedsonite and aegirine have been determined by a JOEL JXA-8100 electron microprobe at the GIG, CAS. To minimize the diffusion of F and Cl, the F, Cl, Na, CaO, and SiO_2 are first tested with an accelerating voltage of 15 kV, a beam current of 15 nA and a beam size of 15 μm (e.g., Andersson et al., 2019). Then an accelerating voltage of 15 kV and a beam current of 20 nA and a beam size of 5 μm are used to test the remaining major elements. The peak and background counting time are 10 s and 5 s for F and Cl, 20 s and 10 s for Ca, P, Si, Fe, Al, and Mg, 60 s and 30 s for Mn, and 7 s and 3 s for Na and K, respectively. The adjustment standards are: apatite for Ca and P, fluorite for F, sodalite for Cl, albite for Na and Si, almandine for Al, orthoclase for K and pyroxene for Mn, Fe, and Mg. The analytical errors were generally less than 1% and the result of apatite standards are listed in Supplementary Table S2.

The trace element compositions of apatite, hornblende, arfvedsonite and aegirine were measured by a resolution M-50 LA system equipped with an Agilent 7900a type ICP-MS at the GIG, CAS. The operating conditions include: energy density of 90 mJ/cm^2, a repetition rate of 6 Hz for each ablation and flow rates of 0.85 L/min for Ar auxiliary gas, 15 L/min for Ar plasma gas and 1.0 L/min for He carrier gas, and 31 μm

laser ablation spot diameter. Each analysis consists of 20 s background test, followed by data acquisition for around 45 s. The Ca concentration analyzed by EPMA for each apatite was used as internal standard (^{43}Ca) for trace elemental calibration of apatite. Standards of BCR-2G, BIR-1G and BHVO-2G were used for trace element calibration of hornblende, arfvedsonite and aegirine without applying internal standardization. The NIST SRM 610 as external standard and NIST SRM 612 as unknown sample were measured twice after a group of eight spot analyses to monitor the quality of analytical data. Detail analytical procedures was reported in Liu et al. (2008). Data reduction was performed off-line by the ICPMSDataCall software (version 10.0). The major and trace element compositions of apatite, hornblende, arfvedsonite and aegirine, and standards of NIST SRM 610 and NIST SRM 612 during this study and the recommended values (Pearce et al. 1997) are listed in Tables S2 – S5, respectively.

H_2O content and H isotope analyses of apatite

The H_2O and H isotopic compositions of apatite were conducted on a Cameca Nano-SIMS 50L at the Institute of Geology and Geophysics (IGG), CAS. The detailed analytical procedure was reported in Hu et al. (2015). The apatite grains after major and trace element analyses were embedded in a tin-based alloy and coated with gold to reduce the background value of water (Xia et al., 2019; Yang et al., 2021). The mounts were loaded into the instrument vacuum chamber and pumped down for 3 days prior to analysis to reduce the influence of background water. During the

289 analysis, a primary Cs^+ ion beam of ~0.5 nA and ~2 μm in diameter with an impact
290 energy of 16 kV was used to impact the surface of the apatite to generate secondary
291 ions. The electron gun (E-gun) was used for electron compensation, and the electron
292 multiplier (EMS) was used to count the secondary ions. Each analysis has 10×50
293 cycles with each cycle containing 64×64 pixels. The default count time for each pixel
294 is 132 s. During the whole test process, the vacuum degree was less than $1\text{-}2\times10^{-10}$torr,
295 and the total analysis time were about 8 mins. The D/H ratios are expressed as: δD (‰)
296 = $1000 \times [(D/H)_{sample}/(D/H)_{SMOW}) - 1)] \times 1000$. The δD values and H_2O contents are
297 corrected by both the mass fractionation of the instrument (IMF = (1000 ×
298 $[D/H_m/D/H_t - 1]$ and the background water of instrument, where D/H_m is the measured
299 result and D/H_t is the recommended value). The standards include Kovdor and
300 Durango apatite, MORB glass and ND 70-01. All glass and apatite standards yielded
301 external errors, which are consistent with the recommended values (Hu et al., 2015
302 and references therein). The analytical results of water and H isotopic compositions of
303 apatite and related standards are respectively listed in Tables S6 and S7.

304 # Results

305 ## Summary of whole-rock and zircon Hf-O isotope geochemistry

306 The whole-rock geochemistry of the Fuzhou I-A-type granitic complex has
307 extensively been studied in the literature (e.g., Martin et al., 1994; Zhao et al., 2016;
308 Chen et al., 2019b; Zhu et al., 2021). The major oxide, trace element compositions
309 and Nd isotope data are listed in Table S1. The I-type granitoids have 61.57 – 76.43

wt% SiO_2, 4.10 – 4.74 wt% K_2O and 3.86– 4.94 wt% Na_2O, while the A-type granites almost have the highest SiO_2 (76.32 – 77.92 wt%) and moderate Na_2O (4.12 – 4.92 wt%) contents (Fig. 3a and Table S1). On an A/CNK vs. A/NK diagram, the samples from A-type granites plot in the peralkaline field (we also name them as peralkaline A-type granites hereafter), whereas I-type granitoids fall into metaluminous to peraluminous field (Fig. 3b). In a 10000×Ga/Al via FeO^T/MgO and FeO^T/(FeO^T+ MgO) via SiO_2 diagrams (Fig. 3c–d), the I- and A-type samples are plotted in the fields of I-type and A-type granites, respectively. The I-type granitoids show enrichments in large ion lithophile elements (LILE, e.g., Rb, Ba, K) and light rare earth elements (LREE) but depletions in HFSE (e.g., Nb, Ta and Ti), Sr and P in the primitive mantle (PM)-normalized incompatible element spidergrams (Fig. 3e). In contrast, the A-type granites are characterized by insignificant Nb−Ta anomalies relative to La in the PM-normalized spidergrams (Fig. 3f), features typically observed in A_1-type granite (Eby, 1990). They also show even stronger Ba, Sr and P depletions than the I-type granitoids (Fig. 3f).

The I-type granitoids show stronger LREE/HREE fractionation in the chondrite-normalized REE patterns (Fig. 3g), somewhat different from the A-type granites that show 'V-shape' REE patterns with more pronounced negative Eu anomalies (Fig. 3h). Both the I-type and A-type granitoids show highly variable Zr concentrations, with Zr ranging from 84 to 307 ppm and 42 to 308 ppm, respectively. The estimated bulk-rock zirconium saturation temperatures (T_{Zr}, Boehnke et al., 2013) are 670 – 805°C and 733 – 835°C respectively for the I-type granitoids and A-type

332 granites (Table S1). Nevertheless, the I-type and A-type granitoids have quite similar
333 whole-rock Nd and zircon O-Hf isotopic compositions, with whole-rock $\varepsilon_{Nd}(t) = -6.6$
334 to –5.2, zircon $\delta^{18}O = 4.9 - 5.8‰$ and $\varepsilon_{Hf}(t) = -0.3$ to 4.1 in I-type granitoids; and
335 whole-rock $\varepsilon_{Nd}(t) = -6.4$ to –2.7, zircon $\delta^{18}O = 4.2 - 5.4‰$ and $\varepsilon_{Hf}(t) = -1.3$ to 3.3 in
336 A-type granites, respectively (Martin et al., 1994; Chen et al., 2019a, b and this study).
337 Chen et al. (2022) proposed that the high-SiO_2 granite components (including the
338 I-type monzogranite and A-type granite) are complementary with the low-SiO_2
339 monzogranites, which represent the crystal cumulates of crust-derived melt.

340 **Microstructures and chemical compositions of apatite**

341 The apatite crystals separated from the Fuzhou I-A-type granitic complex are
342 mostly prismatic, with a grain size ranging from 100 to 200 μm (Fig. 2). They
343 commonly occur as inclusions hosted in the major minerals such as plagioclase,
344 biotite and accessory minerals like ilmenite (Fig. 2), indicating that apatite was an
345 early crystallizing phase. Most apatites display a homogeneous texture in
346 back-scattered electron (BSE) images, only some grains from the peralkaline A-type
347 granite (e.g., 21KQ-05) contain micropores and show weak compositional zonation,
348 such as F, Cl, S, Na and Ce (Fig. 4a and b). Monazite can occasionally be identified in
349 the micropore or along the grain boundary of apatite from the A-type granite (Fig. 4b),
350 indicating a possible role of hydrothermal activity (Zhang et al., 2020).

351 Apatites from both I-type and A-type granitoids are dominated by F-apatite
352 (Fig. 5a), and a broad negative correlation exists between F and Cl contents (Fig. 5b).

353 **I-type granitoids:** Apatites from the I-type granitoids exhibit large
354 compositional ranges such as F (2.05 – 3.58 wt%), SiO_2 (0.07 – 0.75 wt%), Cl (0.001
355 –0.46 wt%), Sr (37 – 353 ppm) and ∑REE (3693 – 14018 ppm). Their
356 chondrite-normalized REE patterns are characterized by pronounced negative Eu
357 anomalies (Eu*/Eu = 0.05 – 0.34), coupled with the synchronous decreases of Sr and
358 LREE/HREE fractionation (Figs. S2a–c and S3a).

359 **A-type granite.** Apatites from the A-type granite have 2.67 – 3.60 wt% F, 0.004
360 – 0.23 wt% Cl, 0.26 – 1.04 wt% SiO_2, 19 – 326 ppm Sr and 6457 – 17338 ppm ∑
361 REE. Relative to the I-type granitoids, the apatites in the A-type granites have higher
362 Ce and ∑REE concentrations (Table S3). Their chondrite-normalized REE patterns
363 are characterized by LREE enrichments relative to HREE with pronounced negative
364 Eu anomalies and right-declining REE pattern [(Eu*/Eu = 0.13 – 0.26); $(La/Yb)_N$ =
365 2.26 – 20.02; Fig. S2d–f). The HREE fractionation (e.g., $(Gd/Yb)_N$ = 4.64 – 0.64)
366 becomes weaker with decreasing Sr (Figs. S2d-f and S3b).

367 **H_2O content and δD variation in apatite**

368 The water contents and H isotope compositions of apatite in the Fuzhou I-A-type
369 granitic complex are listed in Supplementary Table S6. The apatite crystals from this
370 complex show large variations in H_2O (67 – 3892 ppm) and δD (–325 to +1439‰)
371 (Fig. 6a, b). The δD value of apatite changes weakly when the H_2O content is
372 relatively high (H_2O >500 ppm in the I-type granitoids and H_2O >300 ppm in the
373 A-type granites). Once the H_2O content decreases to low levels (i.e., H_2O < 500 ppm

374 in the I-type granitoids and H_2O < 300 ppm in the A-type granites), the δD values
375 strongly fluctuate in both I-type and A-type granitoids (Fig. 6a, b). In addition, there
376 are broadly positive correlations between H_2O of apatite and T_{-Zr} in both I-type and
377 A-type granitoids (Fig. 6c), with the highest T_{-Zr} in Sample 21KQ-02.

378 **I-type granitoids**: Apatites in the I-type granitoids span a range of H_2O from
379 341 to 3892 ppm and a range of δD between +336 and – 325‰, respectively. The
380 apatites from the monzonite have the highest H_2O content (2612 – 3982 ppm) and
381 span a δD range from –110 to +43‰, and those from the granodiorite show a range of
382 H_2O from 2538 to 2905 ppm and a range of δD between – 222 and +6‰. The apatites
383 from the monzogranite have the lowest H_2O content (341 – 1869 ppm) and show the
384 strongest H isotope variation, spanning a δD range from – 325 to +336‰. There are
385 positive correlations between H_2O and Cl, Ce, ∑REE, Sr/Y and La/Sm, whereas a
386 negative correlation exists between H_2O and F (Fig. 7). The H_2O content of apatite
387 generally decreases from monzonite, granodiorite to monzogranite with the increasing
388 degree of differentiation. The most evolved monzogranite sample (e.g., 19JX01 has
389 the highest $SiO_{2\text{-}WR}$ at ~76 wt%) has the lowest H_2O and highest δD.

390 **A-type granites:** Relative to the I-type granitoids, apatites from the A-type
391 granites generally have much lower H_2O content (67 – 1366 ppm) and even larger δD
392 variation (from –251 to +1439‰). Apatite in 21KQ02 has 819 – 1366 ppm H_2O with
393 a range of δD from –220 to +166‰. The H_2O contents and δD values in 21KQ05 are
394 179 – 836 ppm and –251 – +209‰, respectively. Sample 21KQ20/22 contains 67 –
395 216 ppm H_2O and a range of δD between –148 and +1439‰. In particular, the H_2O

contents of apatite from fine-grained A-type granites (e.g., 21KQ20/22), which contain abundant miarolitic cavities, are significantly lower than the other samples.

Following the decrease of H_2O, the Cl in apatite decreases, whereas F, Ce and Σ REE increase (Fig. 7a–d). A broadly positive correlation between H_2O and Sr/Y can be observed, whereas obvious correlation between H_2O and La/Sm is lacking (Fig. 7e–f). A further profile analysis on a single apatite crystal from A-type granite shows that the water content tends to increase against a decrease of δD from the core to rims (Fig. 8).

Compositions of hornblende, arfvedsonite and aegirine

In order to evaluate the role of possible fluid metasomatism that may produce the geochemical variations from the I-type to peralkaline A-type granites, we also performed *in-situ* compositional analyses on hornblende, arfvedsonite and aegirine (Tables S4-5). The hornblende from I-type granitoids contains 0.13 – 0.32 wt% F, 0.07 – 0.14 wt% Cl, 11.8 – 13.9 wt% FeO, 12.9 – 15.1 wt% MgO, 0.67 – 1.53 wt% Na_2O, 0.41 – 0.87 wt% K_2O, 13 – 69 ppm Zr and 3 – 5 ppm Hf. The arfvedsonite from the peralkaline A-type granite has much higher contents of F (2.34 – 4.31 wt%), FeO (20.2 – 26.3 wt%), alkali metals (Na_2O = 7.9 – 9.8 wt%, K_2O = 1.0 – 1.9 wt%) and HFSEs (e.g., Zr = 80 – 329 ppm and Hf = 8 – 50 ppm) than the hornblende in I-type granitoids (Fig. S4). In the A-type granite, arfvedsonite is replaced by aegirine, during which the contents of HFSE, F and alkali metals increase from arfvedsonite to aegirine (Fig. 10).

Discussion

The similar emplacement ages, spatial contact relationships, and similar whole-rock Nd and zircon Hf-O isotope compositions indicate a petrogenetic connection between the I- and A-type granitoids in Fuzhou area. However, the I- and A-type granitoids contain different mineral assemblage and show distinctive trace element concentrations and H_2O content of apatite. In the following text, we will first address the possible effects of the kinetic H diffusion in apatite, magmatic differentiation and fluid metasomatism on the bulk rock and apatite geochemical variations across the Fuzhou granitic complex. Then we perform numerical estimation for the water contents of their parent magmas and modelling of the possible magmatic degassing that led to the water and δD differences between the I- and A-type granitoids. Finally, we propose a comprehensive petrogenetic model to interpret the formation of Fuzhou I-A-type granitic complex.

Hydrogen Diffusion

Hydrogen is the lightest element and diffuses rapidly with a greater diffusivity of proton than deuteron, so apatite may lose H_2O and change its δD value by a few hundreds per mil (‰) over a timescale from several hours to days (Gaetani et al., 2012; Bucholz et al., 2013; Chen et al., 2015). Given the large H_2O variation in each sample, as well as the negative relationship in the H_2O-δD diagrams from the A-type granites when the H_2O contents reach to low values (i.e., $H_2O < 500$ ppm in the I-type granitoids and $H_2O < 300$ ppm in the A-type granites, Fig. 6b), the H_2O variation in

438 apatite within a sample may reflect either the contribution of sub-solidus H diffusion
439 or addition of low-δD hydrothermal fluid or both.

440 If H diffusion is responsible for the variations in H_2O content and δD, then a
441 trend of decreasing H_2O content and δD would be expected from core to rim in the
442 individual apatite crystal (e.g., Stephant et al., 2020). However, the H_2O and H isotope
443 variations within the analyzed apatite from the A-type granite are inconsistent with a
444 transient H diffusion profile (Fig. 8), in which the increasing H_2O and decreasing δD
445 from core to rims were likely attributed to addition of aqueous fluid with low δD
446 value. During the analysis, we also tried to select the center of crystals >100 μm to
447 ensure that the H_2O contents in apatite are not affected by grain size. Accordingly, we
448 suggest that the sub-solids H diffusion has a minor effect on the H_2O content and δD
449 of apatite.

450 **Magmatic differentiation**

451 The variations in both whole-rock geochemistry and apatite H_2O and δD of the
452 Fuzhou granitic complex could be affected by a variety of magmatic evolution
453 processes such as fractional crystallization, magma mixing and crustal assimilation
454 (e.g., Guo et al., 2007, 2013). A significant role of magma mixing can be ruled out
455 since the apatite grains within individual sample have consistent REE patterns (e.g.,
456 Bruand et al., 2014; Fig. S2). This can be further supported by the relatively
457 homogeneous texture of most apatite crystals in the BSE images and insignificant
458 compositional zonation in the elemental mapping results (Figs. 2 and 4; Zhang et al.,

459 2021). Also, the role of crustal assimilation via factional crystallization (AFC) was
460 insignificant in accordance with the following observations: (1) the A-type granites
461 show no Nb-Ta depletion (Fig. 3f), a signature free of assimilation by crustal materials
462 that generally have Nb-Ta depletion (Rudnick and Gao, 2014), (2) zircon populations
463 from both I- and A-type granitoids have mantle-like $\delta^{18}O$ values ($\delta^{18}O$ = 4.9–5.8‰ in
464 I-type granitoids, $\delta^{18}O$ = 4.2–5.4‰ in A-type granite; $\delta^{18}O$ = 5.3 ± 0.3‰ in mantle
465 zircon) (Valley et al., 1998; Chen et al., 2019b), and (3) both rock types have similar
466 and limited variation in whole-rock $\varepsilon_{Nd}(t)$ values ($\varepsilon_{Nd}(t)$ = –6.6 to –5.2 in the I-type
467 granitoids, $\varepsilon_{Nd}(t)$ = – 6.4 to –2.7 in the A-type granites; Martin et al., 1994; Chen et
468 al., 2019a, b and this study).

469 Alternatively, fractional crystallization can affect the water content, but it can
470 hardly change the H isotope ratio of apatite. Within an individual sample, if the
471 apatites crystallize at different magmatic evolution stages, they may contain variable
472 water. Given the incompatibility of H_2O in nominally anhydrous minerals such as
473 feldspar and quartz (Hauri et al., 2006), fractionation of only nominally anhydrous
474 minerals will increase the water content of evolved melt, which crystallizes apatite
475 with higher H_2O contents. In contrast, fractionation of hydrous minerals such as
476 amphibole and biotite may decrease the water content of evolved melt and the
477 crystallizing apatite is thus expected to contain lower H_2O contents (McCubbin et al.,
478 2016; Davidson et al., 2020). The decrease of H_2O from 3892 to 500 ppm with little
479 changed δD value in the apatite of I-type granitoids (Fig. 6a), the positive correlations
480 of H_2O versus Ce, $\sum$REE, Sr/Y and La/Sm (Fig. 7c-f), and a negative correlation

481 between whole-rock Rb/Sr and H_2O in apatite as well (Fig. S5), are consistent with
482 fractionation of mostly hornblende + plagioclase (Martin et al., 1994; Chen et al.,
483 2019b).

484 However, Chen et al. (2022) proposed that the high-silica granite (75–77wt%
485 SiO_2) might represent the extracted melt complementary to the cumulate residues of
486 porphyritic granite (70–73 wt % SiO_2) in the coeval (Cretaceous) felsic complexes
487 from SE China, suggesting that the parent magma of I-type granitoid was represented
488 by monzogranite (73-75 wt% SiO_2). If this is correct, the less evolved I-type
489 granitoids in the Fuzhou complex, including the monzonites and diorite, would have
490 been considered as cumulates of dominantly hornblende and plagioclase. The
491 monzonite is free of crystal accumulation based on petrographic observation (Fig. 2a),
492 instead it may represent a solidified melt rather than a complementary residual
493 cumulate. The REE characteristics in apatite are also inconsistent with an origin of
494 cumulate (Fig. S6a–b). For instance, the crystallizing apatite would have lower REE
495 concentrations and higher Eu/Eu* ratios during plagioclase accumulation. The similar
496 Eu/Eu* ratios and REE variation trends from the monzonite to the most evolved
497 monzogranite in apatite are clearly different from the trends of plagioclase
498 accumulation (Fig. S6a–b). Accordingly, the apatite geochemistry from the I-type
499 granitoids argues against an origin of cumulate for the lowest-SiO_2 monzonite. We
500 therefore select the least evolved monzonite sample (19DY-07) in this complex as the
501 parent magma of I-type granitoid to perform further fractionation modelling on the
502 basis of mineral assemblage and whole-rock chemical compositions (i.e., Rb, Ba, K,

503 Nb, La, Sr, Nd, Zr, Hf, Eu and Yb). We adapt the equation: $C_i^L/C_i^0 = F^{(D-1)}$ of simple
504 fractional crystallization to calculate the elemental concentration of residual magma
505 (Hanson, 1978). The fractional assemblage in the I-type granitoid is composed of
506 plagioclase (61%) + K-feldspar (15%) + biotite (15%) + hornblende (8%) + apatite
507 (1%). The partition coefficients between mineral and melt are listed in Table 1 of
508 Supplementary Materials. The modelling results suggest that the I-type monzogranite
509 could be produced by 30–40% fractionation of the above mineral assemblage (Fig.
510 9a–b), consistent with the observed Sr and P depletions in the PM-normalized
511 spidergrams (Fig. 3e). Nevertheless, when the apatites contain H_2O less than 500 ppm,
512 the correlations between H_2O and Ce, ∑REE and La/Sm are lacking or even opposite
513 to the fractionation trends (Fig. 7c, d and f). This suggests that the change of H_2O in
514 apatite from the I-type granitoids cannot merely be attributed to fractional
515 crystallization.

516 Sample 21KQ-02 has the highest whole-rock and apatite Sr concentrations and
517 H_2O among the A-type granites, we hence consider it as a likely candidate of the
518 parental magma. The fractional assemblage consists of K-feldspar (60%) +
519 plagioclase (28%) + biotite (10%) + apatite (1.5%) ± zircon (<1%). The fractionation
520 modelling results indicate that the peralkaline A-type granite could be produced
521 through 30–40% fractionation of the above mineral assemblage to interpret their Ba,
522 Sr and P depletions in the PM-normalized spidergrams and the lower concentrations
523 of Zr, Hf and HREEs in the more evolved A-type granite (Figs. 3f and 9a, c;
524 21KQ-05). However, this fractionation cannot produce the negative correlation of

525 H_2O with Ce observed in the A-type granite since apatite has the capacity to host most
526 LREE in granitic melt (Fig. 7c) and much higher HFSE and HREE concentrations in
527 some peralkaline A-type granites (19KQ-1 and 6; Fig. 9c).

528 Given the close tempo-spatial relationships, transitional mineral compositions
529 and similar Hf-Nd-O isotope data, one may speculate a differentiation relationship
530 between the I- and A-type granitoids. We compare 21KQ-02 of A-type granite with
531 19FZ-08 of I-type monzogranite, both of which have similar whole-rock Rb, Sr, Ba
532 and Rb/Sr and volatile contents in apatite (Figs. 9d and S5). However, the much
533 higher T_{-Zr}, HFSE and HREE concentrations in 21KQ-02 than 19FZ-08 argue against
534 the formation of A-type granite through a simple differentiation of I-type
535 monzogranite (Figs. 9d and6c). Alternatively, the parent magma of A-type granite
536 might inherit from the I-type monzogranite and experienced high-temperature HFSE
537 and HREE enrichment.

538 **Fluid metasomatism**

539 Most apatite crystals from the I-type granitoids are subhedral-euhedral with a
540 homogeneous texture and chemical composition, reflecting their crystallization in a
541 magmatic system free of hydrothermal activity (e.g., Harlov, 2015). In accordance
542 with Zhang et al. (2020), the apatite leached by hydrothermal fluid contains low
543 LREE concentrations. However, the apatite crystals from the same sample show
544 consistent REE patterns (Fig. S2), also precluding a significant effect of hydrothermal
545 activity.

546 By contrast, the BSE images and compositional mapping of apatite in the A-type
547 granite show a dissolution-regrowth microstructure, in which some apatites display F
548 enrichment, Cl, Na, Ce and S depletions, and the growth of secondary monazite
549 inclusions along the fractures (Fig. 4b). In addition, the arfvedsonite from the A-type
550 granite contains much higher Na_2O, K_2O, F, Cl, Zr and Hf contents than hornblende
551 from the I-type granitoids (Fig. S4a–d), indicating addition of F-rich alkaline fluids
552 during the magmatic evolution of A-type granite. Such fluid metasomatism can be
553 further evidenced by the occurrence of aegirine, which contains even higher
554 concentrations of Na_2O, FeO, F, and HFSEs than arfvedsonite (Fig. 10a–c). The
555 formation of aegirine records coupled dissolution–reprecipitation as a result of
556 decomposition of arfvedsonite via a reaction: $3Na_3Fe_5Si_8O_{22}(OH)_2 + 2H_2O =$
557 $9NaFeSi_2O_6 + 2Fe_3O_4 + 6SiO_2 + 5H_2$ (e.g., Salvi and Williams-Jones, 2006). During
558 the metasomatism, alkali-zircon-silicate fluid can enhance Zr enrichment in Na–
559 Al-silicate-bearing solutions and play an important role in HFSE mobilization (e.g.,
560 Wilke et al., 2012). Although the whole-rock Nd and zircon Hf isotope compositions
561 of A-type granite suggest a crustal origin, the mantle-like zircon O and apatite H
562 isotope compositions indicate a mantle origin for the metasomatic fluids. This is also
563 consistent with the extensional setting of the Fuzhou I-A-type granitic complex,
564 during which intraplate OIB-type basalts were formed in association with the slab
565 tearing of the subducted paleo-Pacific Ocean (e.g., Guo et al., 2021).

566 All these observations indicate that the metasomatic fluid was F-HFSE-REE-rich
567 and alkaline with high temperature, probably released from the alkaline magmas of

mantle origin (e.g., Chen et al., 2019b). Such alkaline F-rich fluids can carry HFSE and REE (e.g., Martin, 2006; Louvel et al., 2022), leading to HFSE and REE enrichment in the A-type granite (Figs. 3f and 11).

In summary, the I-type granitoids and A-type granites were likely derived from a similar parental magma. The initial I-type magma experienced varying degrees of differentiation (hornblende + biotite + plagioclase + K-feldspar + apatite) to form rock types from monzonite through granodiorite to monzogranite. The A-type granite was likely initially inherited from the I-type monzogranitic magma, which underwent F-HFSE-rich alkaline fluid metasomatism, to form the peralkaline granite after varying degrees of fractionation of K-feldspar + plagioclase + biotite + apatite ± zircon.

Estimation of the H_2O content of parental magmas

The H_2O concentration of magma is largely affected by magmatic evolution and degassing processes. To eliminate the effect of magmatic degassing, we select the least evolved and degassed apatite that contains the highest H_2O and lightest H isotope composition to estimate the water content of parent magma in equilibrium with the apatite in each lithology. The candidates include the apatite grain with H_2O = 3892 ppm and $\delta D = -109‰$ in monzonite, H_2O = 2812 ppm and $\delta D = -222‰$ in granodiorite, H_2O = 1869 ppm and $\delta D = -190‰$ in monzogranite, and H_2O = 1223 ppm and $\delta D = -196‰$ in A-type granite, respectively.

The volatile in melt shows a non-Nernstian behaviour, thus the exchange

This is the peer-reviewed, final accepted version for American Mineralogist, published by the Mineralogical Society of America.
The published version is subject to change. Cite as Authors (Year) Title. American Mineralogist, in press.
DOI: https://doi.org/10.2138/am-2023-8936. http://www.minsocam.org/

coefficient (K_d) between apatite and silicate melt is expressed as the following equations based on the thermodynamic model proposed by Li and Costa (2020):

$$\mathrm{Ln}\left(K_{d\ \mathrm{OH\text{-}F}}^{\mathrm{Ap\text{-}melt}}\right) = -\frac{1}{RT}\{94{,}600\ (\pm 5600) - 40(\pm 0.1)\times T + 1000 \times [7(\pm 4) \times (X_F^{Ap} - X_{OH}^{Ap}) - 11(\pm 7) \times X_{Cl}^{Ap}]\} \quad \text{(Eq. 4)}$$

$$\mathrm{Ln}\left(K_{d\ \mathrm{OH\text{-}Cl}}^{\mathrm{Ap\text{-}melt}}\right) = -\frac{1}{RT}\{72{,}900\ (\pm 2900) - 34(\pm 0.3)\times T + 1000 \times [5(\pm 2) \times (X_{Cl}^{Ap} - X_{OH}^{Ap}) - 10(\pm 8) \times X_F^{Ap}]\} \quad \text{(Eq. 5)}$$

Where temperature (T) is in kelvins, the compositions of apatite are expressed in mole fractions ($X_{\mathrm{OH\text{-}F}}^{\mathrm{Ap\text{-}melt}}$), and R is the universal gas. The K_ds are calculated by apatite composition and temperature. Moreover, the mole fraction of F, Cl and OH in the melt can be calculated using the following equations:

$$X_F^{melt} = \frac{\frac{C_F^{melt}}{19}}{\frac{C_{H_2O}^{melt}}{18} + \frac{1 - C_{H_2O}^{melt}}{32.5}} \text{ and } X_F^{melt} = \frac{\frac{C_F^{melt}}{19}}{\frac{C_{H_2O}^{melt}}{18} + \frac{1 - C_{H_2O}^{melt}}{32.5}} \quad \text{(Eq. 6)}$$

$$X_{OH}^{melt} = [OH] = \frac{\frac{1}{2} - \sqrt{\frac{1}{4} - \left\{\left(\frac{K_2 - 4}{K_2}\right)([H_2O_t] - [H_2O_t]^2)\right\}}}{\left(\frac{K_2 - 4}{2K_2}\right)} \quad \text{(Eq. 7)}$$

$$[H_2O_t] = \frac{\frac{C_{H_2O}^{melt}}{18}}{\frac{C_{H_2O}^{melt}}{18} + \frac{1 - C_{H_2O}^{melt}}{W}} \quad \text{(Eq. 8)}$$

Where the equilibrium constant K_2 is usually determined from experiments and spans a range of 0.44–0.52 for dacitic to rhyolitic magmas (Zhang, 1999; Hui et al., 2008). $C_{\mathrm{H_2O}}^{\mathrm{melt}}$ is the mass fraction of total H_2O in melt. W is the molar mass of the dry silicate melt, i.e., ~32.5 g/mol for a rhyolite (Zhang, 1999). The relative errors of the calculated water contents of parental melt are ~30 – 40%. Finally, the H_2O concentrations of melt are converted by mole fraction of OH in melt. The detailed description of the calculation method was described in Li and Costa (2020).

Based on whole-rock halogen analysis and estimations from chemical

610 composition of minerals (such as biotite and hornblende), the previous literature has
611 reported that the I-type granitoids contain12 to 5510 ppm F with an average of ~705
612 ppm, and 9 to 632 ppm Cl with an average of ~198 ppm (Dahlquist et al., 2010; De La
613 Hoz et al., 2014; Morales Càmera et al., 2020, 2022; Zandomeni et al., 2021). The
614 A-type granites have 150 to 30000 ppm F with an average of 4600 ppm, and 10 to
615 2566 ppm Cl with an average of 609 ppm (Bea et al., 2016; Montero et al., 2009;
616 Moreno et al., 2014, 2020; Wang et al., 2018).

617 We compare the measured whole-rock F and Cl contents to the calculated F and
618 Cl concentrations based on partition coefficients of halogens between apatite and
619 rhyolitic magma. The whole-rock F and Cl contents are significantly lower than the
620 calculated halogen concentrations, probably as a consequence of extensive degassing
621 during the magma emplacement. Here we use the highest F and Cl contents of apatite
622 and the partition coefficients between apatite and dacite/rhyolite to estimate the F and
623 Cl contents of parent magmas for the I-type and A-type granitoids, respectively (Table
624 S1). The calculated results show that the parental magma for monzonite has 1870 ppm
625 F and 2295 ppm Cl, 2040 ppm F and 2170 ppm Cl for granodiorite, 2380ppm F and
626 1160ppm Cl for monzogranite, and 2636 ppm F and 1021 ppm Cl for A-type granite.
627 These estimated values are roughly approximate to the measured F and Cl contents of
628 contemporaneous volcanic rocks (dacite and rhyolite; our unpublished data) in SE
629 China and are also comparable with the F and Cl contents reported for other A-type
630 and I-type granites worldwide.

631 The calculation results show that the parent magma contains ~3.0 wt% water for

632 the monzonite, 2.5 wt% water for the granodiorites, 2.3 wt% water for the
633 monzogranite and ~1.8 wt% water for the A-type granite. The estimated water content
634 of parent magma for the monzonite, which has the lowest SiO_2 and highest H_2O,
635 might represent the H_2O concentration of the primary melt for the Fuzhou I-type
636 granitoids.

637 **Magmatic degassing**

638 It has widely been considered that degassing can extensively affect the water
639 content of magmas during the decompression stage (Wallace, 2005; Stephant et al.,
640 2020). The dissolved volatiles escape from the magma during decompression and
641 shallow-level emplacement (e.g., Stock et al., 2018; Peslier et al., 2019), leading to
642 H_2O loss and H isotope fractionation (Taylor and Sheppard, 1986; Wei et al., 2000; De
643 Hoog et al., 2009; Peslier et al., 2019). The variation of δD against H_2O in apatite
644 from both rock types in the Fuzhou granitic complex, in particular when the water
645 contents decrease to hundreds of ppm (e.g., <500 ppm for I-type and <300 ppm for
646 A-type; $\delta D = -62 \sim -24‰$ for bulk silicate earth; $\delta D = -218 - +60‰$ for upper mantle;
647 $\delta D < -218‰$ for deep mantle; Hallis et al., 2015; Robinson et al., 2016; Stephant et al.,
648 2021), could be attributed to magmatic degassing. In the I-type granitoids, degassing
649 may have occurred when the magma becomes highly evolved (e.g., monzogranite)
650 with extensive H isotope fractionation beyond the scope of Rayleigh fractionation. In
651 the case of A-type granite, degassing may have been associated with the development
652 of miarolitic texture and more extensive H isotope fractionation.

Degassing of H_2O will significantly increase the δD and lead to a positive correlation between H_2O and δD in an oxidizing environment (e.g., Davidson et al., 2020; Hu et al., 2020). In contrast, degassing of H_2/CH_4 is expected to form a negative correlation between H_2O and δD under reducing conditions (Demény et al., 2006; Davidson et al., 2020). Extensive (95–98%) degassing of H_2/CH_4 can even increase the δD value by 800–1000‰, as observed in apatite of lunar samples (e.g., Greenwood et al., 2011; Tartèse et al., 2014; Davidson et al., 2020; Hu et a., 2021). The mineral assemblage of the Fuzhou I-A-type granitic complex indicates its formation under a relatively reducing environment (Qiu et al., 1999; Martin et al., 1994), suggesting that the H_2O variations in apatite probably reflect varying degrees of degassing of H_2/CH_4. The effects of degassing on H isotope variation can be calculated theoretically using open and closed systems, respectively (Taylor and Sheppard, 1986; De Hoog et al., 2009; Peslier et al., 2019). As discussed earlier, the narrow δD variation against the decrease of H_2O in the apatite from monzonite to granodiorite can be interpreted by hydrous mineral fractionation. When the water contents decrease to < 2000 ppm in the I-type monzogranite and drop to < 700 ppm in the A-type granites, the extensive δD variations in both I-type and A-type granites suggest an important role of magmatic degassing. In the following text, we conduct the numerical modelling of degassing in the more evolved I-type granite and A-type peralkaline granite. We select the apatite with the highest water content and low δD value from19FZ-08 and 21KQ-05 (H_2O = 1869 ppm, δD = −190‰ and H_2O = 697 ppm, δD = −83‰, respectively), as the initial conditions to evaluate the role of

675 magmatic degassing in I-type and A-type granites, respectively (Fig. 12a and b).

676 The H/D fractionation during the degassing process in an open system follows
677 the law of Rayleigh fractionation:

678 $\delta D = \delta D_0 - (1000+\delta D_0)\times(1-f^{\alpha-1})$; (Eq. 1)

679 The H/D fractionation during degassing in a closed system is expressed as:

680 $\delta D = \delta D_0 - (1-f)\times 1000 \ln\alpha$; (Eq. 2)

681 Where α can be simply calculated from the molecular weight of the H molecular
682 species involved or the H and D atoms that are diffusing from a nominally anhydrous
683 mineral (Roskosz et al., 2016, 2018; Peslier et al., 2019):

684 α^2=W (H species)/W (D species) (Eq.
685 3)

686 with D species and H species as the molecular weights of the species H- and
687 D-bearing species (for example H_2O, DHO, OH, DH, H_2, H and D), degassing of H_2
688 ($M_1 = 2$ for H_2 and $M_2 = 3$ for HD) therefore yields an α value of 0.5 − 0.8, and
689 degassing of H_2O ($M_1 = 18$ for H_2O and $M_2 = 19$ for HDO) yields an α value of about
690 1.0. The modelling results are illustrated in Fig. 12.

691 The apatite crystals in the I-type monzogranites span a range of *f* (the fraction of
692 residual water) from 1.0 to 0.18. About one third of apatite grains plot in the
693 H_2/CH_4-degassing field (on or above the violet line in Fig. 12a), which can be
694 interpreted by closed-system H_2/CH_4 degassing with a range of α from 0.5 to 0.8. The
695 rest of them, which are plotted between the closed-system H_2/CH_4-degassing and
696 open-system H_2O-degassing fields, are likely attributed to Rayleigh H isotope

fractionation following the fractional crystallization of hydrous minerals such as biotite and hornblende (Suzuoki and Epstein, 1976; Graham et al., 1984). The wide H_2O and δD variations in the I-type monzogranite generally favor a closed-system degassing model.

Compared to the I-type granite, the apatite crystals in the A-type granites span a range of *f* from 1.0 to 0.1, indicating a stronger H loss. More than half of apatite grains plot in the H_2/CH_4-degassing field (on or above the violet line in Fig. 12b), which can be interpreted by open-system degassing of H_2/CH_4 with an α range from 0.5 to 0.8, in particular those crystals with δD > +400‰ might experience a loss of H more than 90%. As the water content decreases from 697 ppm to 300 ppm (*f* ranges from 1.0 to 0.3), the δD exhibits slight fractionation, which can be attributed to degassing of H_2/CH_4 in a relatively closed system. Once H_2O in apatite drops below 300 ppm, the stronger δD variations in the A-type granites require more extensive open-system degassing of H_2/CH_4, as indicated from the miarolitic texture.

Therefore, the variable water and H isotope data of apatite from the Fuzhou I-A-type granitic complex likely resulted from varying degrees of magmatic degassing in different systems, i.e., the I-type monzogranites experienced closed-system degassing, whereas the A-type granite underwent stronger open-system degassing (Fig. 12a and b), probably as a result of emplacement at a shallower crustal level. Both kinds of magmatic degassing led to a rapid decrease of H_2O/Ce and an abrupt increase of F/Cl (Fig. 13), which may be potential geochemical indexes to track the magmatic devolatilization.

719 **Implications for A-type granite petrogenesis**

720 The nature of A-type granite is alkaline, anhydrous and anorogenic (e.g., Loiselle
721 and Wones, 1979; Pitcher, 1997; Bonin, 2007). The main petrogenetic models of
722 A-type granite include: (1) highly differentiated melt of mantle-derived magma (e.g.,
723 Kerr and Fryer, 1993; Chen et al., 2022); (2) partial melting of the lower continental
724 crust with specific bulk-rock composition and under specific fluid regimes, including
725 melt of water-poor lower crustal granulite fluxed by F-rich volatiles (e.g.,
726 Landenberger and Collins, 1996); (3) partial melting of a lower crustal source from
727 which melt have been extracted previously (Clemens et al., 1986; Collins et al., 1982);
728 (4) partial melting of tonalitic/granodioritic lower crust (Creaser et al., 1991; Skjerlie
729 and Johnston, 1993; Patiño Douce, 1997); and (5) partial melting of the lower crust
730 metasomatized by alkali-rich mantle-derived fluids that fertilize the crustal source
731 (Martin, 2006).

732 The A-type granite in the Fuzhou granitic complex was unlikely to represent the
733 highly differentiated melt of mantle-derived magmas. Assuming that the
734 mantle-derived magma has 48% SiO_2, mass balance consideration suggests that the
735 fraction of residual magma (F) would be less than 30% to yield the evolved melt with
736 SiO_2 ~76%, as observed in the A-type granites. Such high-degree differentiation
737 requires a large volume of mafic magmas associated with the A-type granites. This is
738 inconsistent with the field observations – few coeval mafic magmas have been found
739 in the Fuzhou area (Chen et al., 2019b, 2022). In addition, the A-type granites from
740 Fuzhou granitic complex have much higher $(Th/Ta)_{PM}$ ratios (1.2–9.5, with an average

741 of 5.5) than mantle values ($(Th/Ta)_{PM} < 1.0$, e.g., Montero et al., 2009), suggesting an
742 insignificant mantle contribution in the petrogenesis.

743 The A-type granite cannot yet be formed through melting of water-poor lower
744 crustal granulites (e.g., Collins et al., 1982). Assuming that the A-type granite (1.8 wt%
745 H_2O) as the primitive magma from the lower crustal granulite, considering the degree
746 of partial melting (such as F=10%) and the incompatibility of water (K_d <0.01), the
747 water content in the source should be less than 0.20 wt%, comparable with the
748 anhydrous mafic granulite with refractory compositions (Xia et al., 2006; Jin et al.,
749 2021). However, most of lower crustal mafic granulite are depleted in Nb and Ta
750 (Rudnick and Gao, 2014), melting of such lower crustal protoliths is unlikely to form
751 felsic magmas with positive Nb-Ta anomalies as observed in these A-type granites
752 (Fig. 3f), even if those mafic granulite protoliths had been melted during the
753 percolation of F-rich volatiles. Similarly, the insignificant Nb-Ta anomalies in the
754 Fuzhou peralkaline A-type granites also preclude their derivation by melting of the
755 coeval I-type granitoids, which also show negative Nb-Ta anomalies in the
756 PM-normalized spidergrams (Fig. 3f).

757 Another possibility is that the I-type and A-type granites were derived from two
758 different crustal sources that have no petrogenetic connection (e.g., Montero et al.,
759 2009). In SE China, underplating of mantle-derived magma caused extensive melting
760 of Proterozoic crust during Mesozoic time, leading to the formation of widespread
761 felsic lavas and intrusive counterparts (e.g., Guo et al., 2012; Chen et al., 2019a and b).
762 If the underplated magmas were strongly alkaline, such as nephelinite and syenite,

763 capable therefore of releasing hydrothermal alkaline fluids to magmatic source, then
764 the resulting magmas would exhibit a peralkaline character to form the peralkaline
765 A-type granite. On the contrary, if the underplated magmas were tholeiitic or
766 moderately alkaline, with little capacity for releasing abundant alkaline fluids, then
767 the resulting magma would be expected to show the features of I-type granite
768 (Montero et al., 2009). This hypothesis could have interpreted the much higher HFSE
769 contents and somewhat higher magma temperatures in the A-type granites than I-type
770 granitoids. However, it is inconsistent with the mineral assemblage and crystallization
771 sequence in A-type granite (Figs. 2g, h and S1c-f), e.g., if the parent magma of A-type
772 granite were peralkaline with A/NK < 1.0, the characteristic minerals such as aegirine
773 and arfvedsonite should have been early crystallizing phases with the absence of
774 plagioclase. This contrasts with the petrographic observations that aegirine and
775 arfvedsonite are late crystallizing phases and frequent plagioclase exists in all A-type
776 granite samples.

777 Alternatively, we favor that the I-type and A-type plutons of the Fuzhou granitic
778 complex were emplaced synchronously and have a close petrogenetic connection, as
779 indicated from their similar whole-rock Nd isotopic compositions and zircon Hf-O
780 isotopic data (Chen et al., 2019a, b, 2022; Table S1). We thus propose a
781 comprehensive petrogenetic model invoking fractional crystallization, fluid
782 metasomatism and magmatic degassing. Under the rollback-tearing of the subducting
783 paleo-Pacific slab (e.g., Guo et al., 2021), underplating of mantle magmas triggered
784 melting of the Proterozoic crust to produce the primary magma of monzonite, which

785 experienced fractionation of hornblende + plagioclase + K-feldspar + apatite coupled
786 with a closed-system degassing to form the granodiorite and monzogranite. The
787 monzogranitic magma was metasomatized by mantle-derived F-HFSE-REE-rich
788 alkaline fluids to produce the peralkaline magma that subsequently underwent
789 K-feldspar + plagioclase + biotite + apatite fractionation via a stronger open-system
790 degassing to form the A-type granites (Fig. 14). This model can well explain the
791 tempo-spatial relationship, mineral assemblage and crystallization sequence, e.g., the
792 similar emplacement age, contact relationship and presence of plagioclase in all I- and
793 A-type granitoids and the late occurrence of arfvedsonite. Apart from the Fuzhou
794 complex, there are several I-A-type granitic complexes (e.g., Qingtian and Taohuadao;
795 Zhao et al., 2016; Gao et al., 2018) along with the Changle-Nan'ao Fault – a major
796 lithosphere-scale fault in SE China (e.g., Wang et al., 2013). The mantle-derived
797 F-HFSE-REE-rich alkaline fluids might percolate the crust along the major fault and
798 metasomatized the I-type magma to form the peralkaline A-type granites. With the
799 absence of such fluid metasomatism, the I-type magma may differentiate to form
800 highly fractionated granites or even peraluminous A-type granites (e.g., Chen et al.,
801 2022).

802 Regardless of magmatic differentiation (e.g., Chen et al., 2019b, 2022), fluid
803 metasomatism and magmatic degassing play important roles to produce the
804 geochemical diversity of the Fuzhou I-A-type granitic complex. Relative to the I-type
805 granitoids, the water-poor nature of A-type granite in the Fuzhou complex was
806 probably attributed to extensive degassing that led to the loss of most H_2O during

807 magma emplacement instead of derivation from a water-poor crustal source as
808 previously thought. Accordingly, our results and petrogenetic interpretations support
809 that peralkaline A-type granite may originate from I-type granitic magma through
810 fluid metasomatism and degassing.
811

812 **ACKNOWLEDGMENTS AND FUNDING**

813 We thank Dr. Sen Hu, Ruiying Li and Jialong Hao for assistance with the
814 Nano-SIMS water and H isotope analyses on apatite, Yonghua Cao, Pengli He for
815 assistance with EPMA analysis, Le Zhang, Yaqian Wen for assistance with
816 LA-ICP-MS analysis, Weicheng Hua for allocation of samples and Yangming Wu for
817 discussion. We are grateful to Associate editor, Dr. A. Acosta-Vigil, Prof. W.J. Collins
818 and two anonymous reviewers for their careful and detailed reviews, comments and
819 suggestions, which greatly help to improve the manuscript. This research was
820 financially supported by National Natural Science Foundation of China (42073032,
821 42021002 and 42103044) and China Postdoctoral Science Foundation
822 (2021M693190).

823 **References cited**

824 Andersson, S.S., Wagner, T., Jonsson, E., Fusswinkel, T., and Whitehouse, M.J. (2019)
825 Apatite as a tracer of the source, chemistry and evolution of ore-forming fluids:
826 The case of the Olserum-Djupedal REE-phosphate mineralisation, SE Sweden.
827 Geochimica et Cosmochimica Acta, 255, 163–187.

828 Bea, F., Montero, P., Haissen, F., Molina, J.F., Michard, A., Lazaro, C., Mouttaqui, A.,
829 Errami, A., and Sadki, O. (2016) First evidence for Cambrian rift-related
830 magmatism in the West African Craton margin: the Derraman Peralkaline Felsic
831 Complex. Gondwana Research, 36, 423–438.
832 Belousova, E.A., Walters, S., Griffin, W.L., and O'Reilly, S.Y. (2001) Trace element
833 signatures of apatite from granitoids of Mount Isa inlier, northwestern Queensland.
834 Australian Journal of Earth Sciences, 48, 603–619.
835 Boehnke, P., Watson, E.B., Trail, D., Harrison, T.M., and Schmitt, A.K. (2013) Zircon
836 saturation rerevisited. Chemical Geology, 351, 324–334.
837 Bonin, B. (2007) A-type granites and related rocks: evolution of a concept, problems
838 and prospects. Lithos, 97, 1–29.
839 Bouvier, A., Vervoort, J.D., and Patchett, P.J. (2008) The Lu-Hf and Sm-Nd isotopic
840 composition of CHUR: constraints from unequilibrated chondrites and
841 implications for the bulk composition of the terrestrial planets. Earth and Planetary
842 Science Letters, 280, 285–295.
843 Bruand, E., Storey, C., and Fowler, M. (2014) Accessory mineral chemistry of high
844 Ba-Sr granites from northern Scotland: constraints on petrogenesis and records of
845 whole-rock signature. Journal of Petrology, 55, 1619–1651.
846 Bruand, E., Fowler, M., Storey, C., and Darling, J. (2017) Apatite trace element and
847 isotope applications to petrogenesis and provenance. American Mineralogist, 102,
848 75–84.
849 Bruand, E., Storey, C., Fowler, M., and Heilimo, E. (2019) Oxygen isotopes in titanite

850 and apatite, and their potential for crustal evolution research. Geochimica et
851 Cosmochimica Acta, 255, 144–162.
852 Bucholz, C.E., Gaetani, G.A., Behn, M.D., and Shimizu, N. (2013) Post-entrapment
853 modification of volatiles and oxygen fugacity in olivine-hosted melt inclusions.
854 Earth and Planetary Science Letters, 374, 145–155.
855 Cao, M.J., Evans, N.J., Hollings, P., Cooke, D., McInnes, B.I.A., and Qin, K.Z. (2021)
856 Apatite texture, composition, and O-Sr-Nd isotope signatures record magmatic
857 and hydrothermal fluid characteristics at the Black Mountain porphyry deposit,
858 Philippines. Economic Geology, 116, 1189–1207.
859 Chappell, B.W., and White, A.J.R. (1992) I- and S-type granites in the Lachlan Fold
860 Belt. Earth and Environmental Science Transactions of the Royal Society of
861 Edinburgh, 83, 1–26.
862 Clemens, J.D., Holloway, J.R., and White, A.J.R. (1986) Origin of an A-type granite:
863 experimental constraints. American Mineralogist, 71, 317–324.
864 Chen, J.Y., Yang, J.H., Zhang, J.H., Sun, J.F., and Wilde, S.A. (2013) Petrogenesis of
865 the Cretaceous Zhangzhou batholith in southeastern China: Zircon U-Pb age and
866 Sr-Nd-Hf-O isotopic evidence. Lithos, 162-163, 140–156.
867 Chen, J.Y., Yang, J.H., and Zhang, J.H. (2019a) Multiple sources of Cretaceous
868 granitoids in northeastern Fujian, coastal area of southeastern China. Journal of
869 Asian Earth Sciences, 182, 103939.
870 Chen, J.Y., Yang, J.H., and Zhang, J.H. (2019b) Origin of Cretaceous aluminous and
871 peralkaline A-type granitoids in northeastern Fujian, coastal region of southeastern

872 China. Lithos, 340–341, 223–238.

873 Chen, J.Y., Yang, J.H., Zhang, J.H., Sun, J.F., Zhu, Y.S., and Hartung, E. (2022)
874 Generation of cretaceous high-silica granite by complementary crystal
875 accumulation and silicic melt extraction in the coastal region of southeastern
876 China. Geological Society of America Bulletin, 134, 201–222.

877 Chen, Y., Zhang, Y.X, Liu, Y., Guan, Y.B., Eiler, J., and Stolper E.M. (2015) Water,
878 fluorine, and sulfur concentrations in the lunar mantle. Earth and Planetary
879 Science Letters, 427, 37–46.

880 Chu, M.F., Wang, K.L., Griffin, W.L., Chung, S.L., O'Reilly, S.Y., Pearson, N.J., and
881 Iizuka, Y. (2009) Apatite Composition: Tracing Petrogenetic Processes in
882 Transhimalayan Granitoids. Journal of Petrology, 50, 1829–1855.

883 Collins, W.J., Beams, S.D., White, A.J.R., and Chappell, B.W. (1982) Nature and
884 origin of A-type granites with particular reference to southeastern Australia.
885 Contributions to Mineralogy and Petrology, 80, 189–200.

886 Collins, W.J., Huang, H.Q., Bowden, P., and Kemp, A. (2019) Repeated S–I–A-type
887 granite trilogy in the Lachlan Orogen and geochemical contrasts with A-type
888 granites in Nigeria: implications for petrogenesis and tectonic discrimination.
889 Geological Society London Special Publications, 2019, 491, SP491-2018–159.

890 Condie, K. C., Pisarevsky, S. A., Puetz, S. J., Roberts, N.M.W., and Spencer, C. J.
891 (2023) A-type granites in space and time: Relationship to the supercontinent cycle
892 and mantle events. Earth and Planetary Science Letter, 610, 118125.

893 Creaser, R.A., and White, A.J.R. (1991) Yardea Dacite—Large-volume,

894 high-temperature felsic volcanism from the Middle Proterozoic of South Australia.
895 Geology, 19, 48–51.
896 Dahlquist, J.A., Alasino, P.H., Eby, G.N., Galindo, C., and Casquet, C. (2010) Fault
897 controlled Carboniferous A-type magmatism in the proto-Andean foreland
898 (Sierras Pampeanas, Argentina): geochemical constraints and petrogenesis. Lithos,
899 115, 65–81.
900 Dall'Agnol, R., Scaillet, B., and Pichavant, M. (1999) An experimental study of a
901 Lower Proterozoic A-type granite from the Eastern Amazonian Craton, Brazil.
902 Journal of Petrology, 40, 1673–1698.
903 Davidson, J., Wadhwa, M., Hervig, R.L., and Stephant, A. (2020) Water on mars:
904 insights from apatite in regolith breccia northwest Africa 7034. Earth and
905 Planetary Science Letters, 552, 116597.
906 Demény, A., Vennemann, T.W., Harangi, S., Homonnay, Z., and Fórizs, I. (2006)
907 H_2O– δD–Fe_{III} relations of dehydrogenation and dehydration processes in
908 magmatic amphiboles. Rapid Communications in Mass Spectrometry, 20, 919–
909 925.
910 De Hoog, J.C.M., Taylor, B.E., and Bergen, M.J.V. (2009) Hydrogen-isotope
911 systematics in degassing basaltic magma and application to Indonesian arc basalts.
912 Chemical Geology, 266, 256–266.
913 De la Hoz, M., Coniglio, J., Kirschbaum, A. (2014) El Granito Los Ratones como-
914 posible Fuente de flúoren la formaciòn de sistemas epitermales, Sierra de
915 Fiambala, Catamarca. Serie Correlacion Geologica, 30, 77–91.

916 Eby, G.N. (1990) The A-type granitoids: a review of their occurrence and chemical
917 characteristics and speculations on their petrogenesis. Lithos, 26, 115–134.
918 Farahat, E.S., Mohamed, H.A., Ahmed, A.F., and Mahallawi, M.M.E. (2007) Origin
919 of I- and A-type granitoids from the Eastern Desert of Egypt: Implications for
920 crustal growth in the northern Arabian-Nubian Shield. Journal of Asian Earth
921 Sciences, 49, 43–58.
922 Gaetani, G.A., O'Leary, J.A., Shimizu, N., Bucholz, C.E., and Newville, M. (2012)
923 Rapid reequilibration of H_2O and oxygen fugacity in olivine-hosted melt
924 inclusions. Geology, 40, 915– 918.
925 Gao, Y.Y., Griffin, W.L., Chu, M.F., O'Reilly, S.Y., Pearson, N.J., Li, Q.L., Liu, Y.,
926 Tang, G.Q., and Li, X.H. (2018) Constraints from zircon Hf-O-Li isotopic
927 compositions on the genesis of slightly low-$\delta^{18}O$ alkaline granites in the
928 Taohuadao area, Zhejiang Province, SE China. Journal of Asian Earth Sciences,
929 167, 197–208.
930 Geng, H.Y., Sun, M., Yuan, C., Xiao, W.J., Xian, W.S., Zhao, G.C., Zhang, L.F., Wong,
931 K.N., and Wu, F.Y. (2009) Geochemical, Sr–Nd and zircon U–Pb-Hf isotopic
932 studies of Late Carboniferous magmatism in the West Junggar, Xinjiang:
933 implications for ridge subduction? Chemical Geology, 266, 364–389.
934 Graham, C.M., Harmon, R.S., and Sheppard, S.M.F. (1984) Experimental hydrogen
935 isotope studies: hydrogen isotope exchange between amphibole and water.
936 American Mineralogist, 69, 128–138.
937 Greenwood, J.P., Itoh, S., Sakamoto, N., Warren, P., Taylor, L., and Yurimoto, H.

938 (2011) Hydrogen isotope ratios in lunar rocks indicate delivery of cometary water
939 to the moon. Nature Geoscience, 4, 79–82.
940 Griffin, W.L., Wang, X., Jackson, S.E., Pearson, N.J., and O'Reilly, S.Y. (2002) Zircon
941 geochemistry and magma mixing, SE China: in-situ analysis of Hf isotopes,
942 Tonglu and Pingtan igneous complexes. Lithos, 61, 237–269.
943 Guo, F., Nakamura, E., Fan, W.M., Kobayashi, K., Li, C.W. (2007) Generation of
944 Palaeocene Adakitic Andesites by Magma Mixing; Yanji Area, NE China. Journal
945 of Petrology, 48, 661–692.
946 Guo, F., Fan, W.M., Li, C.W., Zhao, L., Li, H.X., and Yang, J.H. (2012) Multi-stage
947 crust-mantle interaction in SE China: Temporal, thermal and compositional
948 constraints from the Mesozoic felsic volcanic rocks in eastern Guangdong-Fujian
949 provinces. Lithos, 150, 62–84.
950 Guo, F., Guo, J.T., Wang, C.Y., Fan, W.M., Li, C.W., Zhao, L., Li, H.X., Li, J.Y. (2013)
951 Formation of mafic magmas through lower crustal AFC processes — An example
952 from the Jinan gabbroic intrusion in the North China Block. Lithos, 179, 157-174.
953 Guo, F., Wu, Y.M., Zhang, B., Zhang, X.B., Zhao, L., and Liao J. (2021) Magmatic
954 responses to Cretaceous subduction and tearing of the paleo-Pacific Plate in SE
955 China: An overview. Earth Science Review, 212,103448.
956 Hallis, L. J., Huss, G. R., Nagashima, K., Taylor, G. J., Halldo´rsson, S. A., Hilton, D.
957 R., Mottl, M. J., and Meech K. J. (2015) Evidence for primordial water in Earth's
958 deep mantle. Science, 350, 795–797
959 Hanson, G.N. (1978) The application of trace element to the petrogenesis of igneous

960 rocks of granitic composition. Earth and Planetary Science Letters, 38, 26–43.

961 Hao, L.L., Wang, Q., Wyman, D.A., Ma, L., Wang, J., Xia, X.P., and Qi, Y. (2019)
962 First identification of postcollisional A-type magmatism in the Himalayan-Tibetan
963 orogen. Geology, 47, 187–190.

964 Harlov, D.E. (2015) Apatite: a fingerprint for metasomatic processes. Elements, 11,
965 171–176.

966 Hauri, E.H., Gaetani, G.A., and Green, T.H. (2006) Partitioning of water during
967 melting of the Earth's upper mantle at H_2O-undersaturated conditions. Earth and
968 Planetary Science Letters, 248, 715–734.

969 He, P.L., Huang, X.L., Yang, F., and Wang, X. (2020) Mineralogy constraints on
970 magmatic processes controlling adakitic features of early Permian
971 high-magnesium diorites in the western Tianshan Orogenic Belt. Journal of
972 Petrology, 61, 10.1093/petrology/egaa114.

973 Hu, S., Lin, Y.T., Zhang, J.C., Hao, J.L., Yang, W., and Deng, L.W. (2015)
974 Measurements of water content and D/H ratio in apatite and silicate glasses using
975 a Nano SIMS 50L. Journal of Analytical Atomic Spectrometry, 30, 967–978.

976 Hu, S., Lin, Y.T., Zhang, J.C., Hao, J.L., Yamaguchi, A., Zhang, T., Yang, W., and
977 Changela, H. (2020) Volatiles in the Martian crust and mantle: Clues from the
978 NWA 6162 shergottite. Earth and Planetary Science Letters, 530, 115902.

979 Hu, S., He, H.C., Ji, J.L., Lin, Y.T., Hui, H.J., Anand, M., Tartese, R., Yan, Y.H., Hao,
980 J.L., Li, R.Y., Gu, L.X., Guo, Q., He, H.Y., and Ouyang, Z.Y. (2021) A dry lunar
981 mantle reservoir for young mare basalts of Chang'e-5. Nature, 600, 49–53.

982 Huang, F.F., Scaillet, B., Wang, R.C., Erdmann, S., Chen, Y., Faure, M., Liu, H.S., Xie,
983 L., Wang, Bo., and Zhu, J.C. (2019) Experimental constraints on intensive
984 crystallization parameters and fractionation in A‐type granites: A case study on
985 the Qitianling Pluton, South China. Journal of Geophysical Research: Solid Earth,
986 124,132–10.
987 Huang, X., Sun, S., De Paolo, D. J., and Wu, K. (1986) Nd-Sr isotope study of
988 Cretaceous magmatic rocks from Fujian province. Acta Petrological Sinica, 2,
989 50-61 (in Chinese with English abstract).
990 Hui, H.J., Zhang, Y.X., Xu, Z.J., and Behrens, H. (2008) Pressure dependence of the
991 speciation of dissolved water in rhyolitic melts. Geochimica et Cosmochimica
992 Acta, 72, 3229–3240.
993 Holtz, F., Johannes, W., Tamic, N., and Behrens, H. (2001) Maximum and minimum
994 water contents of granitic melts generated in the crust: a reevaluation and
995 implications. Lithos, 56, 1 –14.
996 Jin, T.L., Wang. Q., Shatsky, V., and Liao, Y. (2021) Water Content and Deformation
997 of the Lower Crust beneath the Siberian Craton: Evidence from Granulite
998 Xenoliths. Journal of Geology, 129, 475–498.
999 Kerr, A., and Fryer, B.J. (1993) Nd isotope evidence for crust-mantle interaction in the
1000 generation of A-type granitoid suites in Labrador, Canada. Chemical Geology, 104,
1001 39–60.
1002 Kusebauch, C., John, T., Whitehouse, M.J., Klemme, S., and Putnis, A. (2015)
1003 Distribution of halogens between fuid and apatite during fuidmediated

1004 replacement processes. Geochimica et Cosmochimica Acta, 170, 225–246.

1005 Ladenburger, S., Marks, M.A.W., Upton, B., Hill, P., Wenzel, T., and Markl, G. (2016)
1006 Compositional Variation of Apatite from Rift-Related Alkaline Igneous Rocks of
1007 the Gardar Province, South Greenland. American Mineralogist, 101, 612–626.

1008 Landenberger, B., and Collins, W.J. (1996) Derivation of A-type granites from a
1009 dehydrated charnockitic lower crust: evidence from the chaelundi complex,
1010 eastern australia. Journal of Petrology, 37, 145–170.

1011 Li, W.R., and Costa, F. (2020) A thermodynamic model for F-Cl-OH partitioning
1012 between silicate melts and apatite including non-ideal mixing with application to
1013 constraining melt volatile budgets. Geochimica et Cosmochimica Acta, 269, 203–
1014 222.

1015 Li, X.H., Li, Z.X., Wingate, M.T.D., Chung, S.L., Liu, Y., Lin, G.C., and Li, W.X.
1016 (2006) Geochemistry of the 755 Ma Mundine Well dyke swarm, northwestern
1017 Australia: part of a Neoproterozoic mantle superplume beneath Rodinia?
1018 Precambrian Research, 146, 1–15.

1019 Li, X.H., Li, W.X., Li, Z.X., Lo, C.H., Wang, J., Ye, M.F., and Yang, Y.H. (2009)
1020 Amalgamation between the Yangtze and Cathaysia Blocks in South China:
1021 Constraints from SHRIMP U-Pb zircon ages, geochemistry and Nd-Hf isotopes of
1022 the Shuangxiwu volcanic rocks. Precambrian Research, 174, 117–12.

1023 Lin, Q.C., Cheng X.W., Zhang, Y.Q., and Wang, F.Y. (2011) Evolution of granitoids in
1024 the active continental margin: a case study of the Fuzhou compound complex.
1025 Acta Geologica Sinica, 85, 1128–1133.

1026 Liu, L., Qiu, J.S., and Yang, Z.L. (2013) Petrogenesis of the Maoliling pluton in
1027 Linhai County, Zhejiang Province: Constraints from geochronology，
1028 geochemistry and Sr-Nd-Hf isotopes. Acta Petrologica Sinica, 29, 4069－4086
1029 (in Chinese with English abstract).
1030 Liu, L., Hu, R.Z., Zhong, H., Tang, Y.W., Yang, J.H., Li, Z., Zhao, J.L., and Shen, N.
1031 P. (2018) New constraints on the Cretaceous geodynamics of paleo-Pacific plate
1032 subduction: Insights from the Xiaojiang–Beizhang granitoids, Zhejiang Province,
1033 southeast China. Lithos, 314, 382－399.
1034 Liu, Q., Yu, J.H., Wang, Q., Su, B., Zhou, M.F., Xu, H., and Cui, X. (2012) Ages and
1035 geochemistry of granites in the Pingtan–Dongshan Metamorphic Belt, Coastal
1036 South China: new constraints on Late Mesozoic magmatic evolution. Lithos, 150,
1037 268－286.
1038 Liu, Y., Liu, H.C., and Li, X.H. (1996) Simultaneous and precise determination of 40
1039 trace element elements using ICP-MS. Geochimica, 25, 552–558 (in Chinese with
1040 English abstract).
1041 Liu, Y.S., Hu, Z.C., Gao, S., Gunther, D., Xu, J., Gao, C.G., and Chen, H.H. (2008) In
1042 situ analysis of major and trace elements of anhydrous minerals by LA-ICP-MS
1043 without applying an internal standard. Chemical Geology, 257, 34–43.
1044 Louvel, M., Etschmann, B., Guan, Q.S., Testemale, D., and Brugger, J. (2022)
1045 Carbonate complexation enhances hydrothermal transport of rare earth elements in
1046 alkaline fluids. Nature Communications, 13, 1456.
1047 Loiselle, M.C., and Wones, D.R. (1979) Characteristics and origin of anorogenic

granites. Abstracts of papers to be presented at the Annual Meetings of the Geological Society of America and Associated Societies, San Diego, California, November 5–8, vol. 11, p. 468.

Lugmair, G.W., and Marti, K. (1977) Sm-Nd-Pu timepieces in the Angra dos Reis meteorite. Earth and Planetary Science Letters, 35, 273–284.

Mao, M., Rukhlov, A.S., Rowins, S.M., Spence, J., and Coogan, L.A. (2016) Apatite trace element compositions: A robust new tool for mineral exploration. Economic Geology, 111, 1187–1222.

Martin, H., Bonin, B., Capdevila, R., Jahn, B.M., Lameyre, J., and Wang, Y. (1994) The Kuiqi peralkaline granitic complex (SE China): petrology and geochemistry. Journal of Petrology, 35, 983–1105.

Martin, R.F. (2006) A-type granites of crustal origin ultimately result from open-system fenitization-type reactions in an extensional environment. Lithos, 91, 125–136.

McCubbin, F.M., Boyce, J.W., Srinivasan, P., Santos, A.R., Elardo, S.M., Filiberto, J., Steele, A., and Shearer, C.K. (2016) Heterogeneous distribution of H_2O in the Martian interior: implications for the abundance of H_2O in depleted and enriched mantle sources. Meteoritics Planetary Science, 51, 2036–2060.

Montero, P., Bea, F., Corretge, L.G., Floor, P., and Whitehouse, M.J. (2009) U-Pb ion microprobe dating and Sr-Nd isotope geology of the Galiñeiro Intrusive Complex: A model for the peraluminous/peralkaline duality of the Cambro-Ordovician magmatism of Iberia. Lithos 107, 227–238.

1070 Morales Càmera, M.M., Dahlquist, J.A., García-Arias, M., Moreno, J.A., Galindo, C.,
1071 Basei, M.A.S., and Molina, J.F. (2020) Petrogenesis of the F-rich peraluminous
1072 A-type granites: an example from the devonian achala batholith (Characato
1073 Suite), Sierras Pampeanas, Argentina. Lithos, 378-379, 105792.
1074 Morales Cámera, M.M., Dahlquist, J.A., Moreno, J.A., Zandomeni, P.S., García-Arias,
1075 M., and Basei, M.A.S. (2022) The Andaluca plutonic unit, Vinquis Intrusive
1076 Complex, Argentina: An assessment of mantle role inthe genesis of Early
1077 Carboniferous weakly peraluminous A-type granites in the pre-Andean SW
1078 Gondwana margin. Lithos, 106873.
1079 Moreno, J.A., Molina, J.F., Montero, P., Abu Anbar, M., Scarrow, J.H., Cambeses, A.,
1080 and Bea, F. (2014) Unraveling sources of A-type magmas in juvenile continental
1081 crust: constraints from compositionally diverse Ediacaran post-collisional
1082 granitoids in the Katerina Ring Complex, southern Sinai, Egypt. Lithos, 192–195,
1083 56–85.
1084 Moreno, J.A., Dahlquist, J.A., Morales Càmera, M.M., Alasino, P.H., Larrovere, M.A.,
1085 Basei, M.A.S., Galindo, C., Zandomeni, P.S., and Roche, S. (2020)
1086 Geochronology and geochemistry of the Tabaquito batholith (Frontal Cordillera,
1087 Argentina): geodynamic implications and temporal correlations in the SW
1088 Gondwana margin. Journal Geology Society, 177, 455–474.
1089 O'Neil, J.R., and Chappell B .W. (1977) Oxygen and hydrogen isotope relations in the
1090 Berridale batholith. Journal of the Geological Society, 133, 559–57.
1091 Pan, Y.M., and Fleet, M.E. (2002) Compositions of the Apatite-Group Minerals:

1092 Substitution Mechanisms and Controlling Factors. Reviews in Mineralogy and
1093 Geochemistry, 48, 13–49.
1094 Pearce, N.J.G, Perkins, W.T., Westgate, J.A, Gorton, M.P., Jackson, S.E, Neal, C.R.,
1095 and Chenery, S.P. (1997) A compilation of new and published major and trace
1096 element data for NIST SRM 610 and NIST SRM 612 glass reference materials.
1097 Geostandards and Geoanalytical Research, 21, 115–144.
1098 Patiño Douce, A.E. (1997) Generation of metaluminous A-type granitoids by
1099 low-pressure melting of calc-alkaline granitoids. Geology, 25, 743–746.
1100 Peslier, A.H., Hervig, R., Yang, S., Humayun, M., Barnes, J.J., Irving, A.J., and
1101 Brandon, A.D. (2019) Determination of the water content and D/H ratio of the
1102 Martian mantle unravelling degassing and crystallisation effects in nakhlites.
1103 Geochimica et Cosmochimica Acta, 266, 382–415.
1104 Pitcher, W.S. (1997) The Nature and Origin of Granite. 2nd edition. Chapman & Hall,
1105 London, pp. 386.
1106 Qiu, J. S., Wang, D.Z., and Mclnnes, B.I.A. (1999) Geochemistry and petrogenesis of
1107 the I- and A-type composite granite masses in the coastal area of Zhejiang and
1108 Fujian Provinces. Acta Petrologica Sinica, 15, 237–246 (In Chinese with English
1109 abstract).
1110 Robinson. K. L., Barnes. J. J., Nagashima. K., Thomen. A., Franchi. I. A., Huss. G. R.,
1111 Anand. M., and Taylor. G. J. (2016) Water in evolved lunar rocks: Evidence for
1112 multiple reservoirs. Geochimica et Cosmochimica Acta, 188, 244–260.
1113 Roskosz, M., Laurent, B., Leroux, H., and Remusat, L. (2016) Experimental

1114 investigation of irradiation-driven hydrogen isotope fractionation in analogs of
1115 protoplanetary hydrous silicate dust. Astrophysical Journal, 832, 55.
1116 Roskosz, M., Deloule, E., Ingrin, J., Depecker, C., Laporte, D., Merkel, S., Remusat,
1117 L., and Leroux, H. (2018) Kinetic D/H fractionation during hydration and
1118 dehydration of silicate glasses, melts and nominally anhydrous minerals.
1119 Geochimica et Cosmochimica Acta, 233, 14–32.
1120 Rudnick, R.L., and Gao, S. (2014) Composition of the continental crust. In: Holland,
1121 H.D., Turekian, K.K. (Eds.), Treatise on Geochemistry, Second edition, Elsevier
1122 Ltd., Amsterdam, pp. 1–51.
1123 Salvi, S., and Williams-Jones A.E. (2006) Alteration, HFSE mineralisation and
1124 hydrocarbon formation in peralkaline igneous systems: Insights from the Strange
1125 Lake Pluton, Canada. Lithos, 91, 19–34.
1126 Sha, L.K., and Chappell, B.W. (1999) Apatite chemical composition, determined by
1127 electron microprobe and laser-ablation inductively coupled plasma mass
1128 spectrometry, as a probe into granite petrogenesis. Geochimica et Cosmochimica
1129 Acta, 63, 3861–3881.
1130 Shaw, D.W. (1972) The origin of apsley gneiss, Ontario. Canadian Journal of Earth
1131 Sciences, 9, 18–25.
1132 Stephant, A., Anand, M., Tartèse, R., Zhao, X., Degli-Alessandrini, G., and Franchi, I.
1133 A. (2020) The hydrogen isotopic composition of lunar melt inclusions: An
1134 interplay of complex magmatic and secondary processes. Geochimica et
1135 Cosmochimica Acta, 284, 196–221.

1136 Stephant, A., Wadhwa, M., Hervig, R., Bose, M., Zhao, X., Barrett, T.J., Anand, M.,
1137 and Franchi. I.A. (2021) A deuterium-poor water reservoir in the asteroid 4 Vesta
1138 and the inner solar system. Geochimica et Cosmochimica Acta, 297, 203–224.
1139 Stock, M.J., Humphreys, M.C.S., Smith, V.C., Isaia, R., Brooker, R.A., Pyle, R.A.,
1140 and Pyle, D.M. (2018) Tracking volatile behaviour in sub-volcanic plumbing
1141 systems using apatite and glass: Insights into pre-eruptive processes at Campi
1142 Flegrei, Italy. Journal of Petrology, 59, 2463–2492.
1143 Sun, C.Y., Cawood, P.A., Xu, W.L., Zhang, X.M., Tang, J., Li, Y., Sun, Z.X., and Xu,
1144 T. (2022) In situ geochemical composition of apatite in granitoids from the eastern
1145 Central Asian Orogenic Belt: A window into petrogenesis. Geochimica et
1146 Cosmochimica Acta, 317, 552–573.
1147 Sun, S.S., and McDonough, W.F. (1989) Chemical and isotopic systematics of oceanic
1148 basalts: Implications for mantle composition and processes. In: Saunders, A.D.,
1149 Norry, M.J. (eds.), Magmatism in the Ocean Basins. Geological Society of
1150 London Special Publication, 42, 315–345.
1151 Suzuoki, T., and Epstein, S. (1976) Hydrogen isotope fractionation between
1152 OH-bearing minerals and water. Geochimica et Cosmochimica Acta, 40, 1229–
1153 1240.
1154 Tartèse, R., Anand, M., Joy, K.H., and Franchi, I.A. (2014) H and Cl isotope
1155 systematics of apatite in brecciated lunar meteorites Northwest Africa 4472,
1156 Northwest Africa 773, Sayh al Uhaymir 169, and Kalahari 009. Meteoritics
1157 Planetary Science, 49, 2266–2289.

1158 Tang, G.J., Wang, Q., Wyman, D.A., Li, Z.X., Zhao, Z.H., Jia, X.H., and Jiang, Z.Q.
1159 (2010) Ridge subduction and crustal growth in the Central Asian Orogenic Belt:
1160 evidence from Late Carboniferous adakites and high-Mg diorites in the western
1161 Junggar region, northern Xinjiang (west China). Chemical Geology, 227, 281–
1162 300.
1163 Tang, G.J., Wang, Q., Wyman, D.A., Li, Z.X., Zhao, Z.H., and Yang, Y.H. (2012) Late
1164 Carboniferous high $\varepsilon_{Nd}(t) - \varepsilon_{Hf}(t)$ granitoids, enclaves and dikes in western
1165 Junggar, NW China: ridge-subduction-related magmatism and crustal growth.
1166 Lithos, 140–141, 86–102.
1167 Taylor, H.P., and Sheppard, S.M.F. (1986) Igneous rocks: I. Processes of isotopic
1168 fractionation and isotopic systematics. In: Valley J. W., Taylor H. P. and O'Neil J.
1169 R. (eds.), Stable isotopes. Mineralogical Society of America, pp. 227–272.
1170 Teiber, H., Marks, M.A.W., Wenzel, T., Siebel, W., Altherr, R., and Markl, G. (2014)
1171 The distribution of halogens (F, Cl, Br) in granitoid rocks. Chemical Geology,
1172 374–375, 92–109.
1173 Tollari, N., Barnes, S. J., Cox, R.A., and Nabil, H. (2008) Trace element
1174 concentrations in apatite from the Sept-Îles intrusive suite, Canada–implications
1175 for the genesis of nelsonites, Chemical Geology, 252, 180–190.
1176 Thomas, R., and Davidson, P. (2012) Water in granite and pegmatite-forming melts.
1177 Ore Geology Reviews, 46, 32–46.
1178 Turner, S.P., Foden, J.D., and Morrison, R.S. (1992) Derivation of some A-type
1179 magmas by fractionation of basaltic magma: an example from the Padthaway

Ridge, South Australia. Lithos, 28, 151–179.

Valley, J.W., Kinny, P.D., Schulze, D.J., and Spicuzza, M.J.(1989) Zircon megacrysts from kimberlite: Oxygen isotope variability among mantle melts. Contributions to Mineralogy and Petrology, 1998, 133, 1–11.

Wallace, P.J. (2005) Volatiles in subduction zone magmas: concentrations and fluxes based on melt inclusion and volcanic gas data. Journal of Volcanology Geothermal Research, 140, 217–240.

Wang, L.X., Ma, C.Q., Zhang, C., Zhu, Y.X., and Marks, M.A.W. (2018) Halogen geochemistry of I and A-type granites from Jiuhuashan Region (South China): insights into the elevated fluorine in A-type granite. Chemical Geology, 478, 164–182.

Wang, Y.J., Fan, W.M., Zhang, G.W., and Zhang, Y.H. (2013) Phanerozoic tectonics of the South China Block: Key observations and controversies. Gondwana Research, 23, 1273–1305.

Wilke, M., Schmidt, C., Dubrail, J., Appel, K., Borchert, M., Kvashnina, K., and Manning, C.E. (2012) Zircon solubility and zirconium complexation in $H_2O+Na_2O+SiO_2\pm Al_2O_3$ fluids at high pressure and temperature. Earth Planet Science Letter, 349-350, 15–25.

Wei, C.S., Zheng, Y.F., and Zhao, Z.F. (2000) Hydrogen and oxygen isotope geochemistry of A-type granites in the continental margins of eastern China. Tectonophysics, 328, 205–227.

Weis, D., Kieffer, B., Maerschalk, C., Pretorius, W., and Barling, J. (2005)

1202 High-precision Pb-Sr-Nd-Hf isotopic characterization of USGS BHVO-1 and
1203 BHVO-2 reference materials. Geochemistry, Geophysics, Geosystems, 6, Q02002.
1204 Whalen, J.B., Currie, K.L., and Chappell, B.W. (1987) A-type granites: geochemical
1205 characteristics, discrimination and petrogenesis. Contributions to Mineralogy and
1206 Petrology, 95, 407–419.
1207 Xia, X.P., Cui, Z.X., Li, W.C., Zhang, W.F., Yang, Q., Hui, H.J., and Lai, C.K. (2019)
1208 Zircon water content: Reference material development and simultaneous
1209 measurement of oxygen isotopes by SIMS. Journal of Analytical Atomic
1210 Spectrometry, 34, 1088–1097.
1211 Xia, Q.K., Yang, X.Z., Deloule, E., Sheng, Y.M., and Hao, Y.T. (2006) Water in the
1212 lower crustal granulite xenoliths from Nushan, eastern China. Journal of
1213 Geophysical Research, 111, B11202.
1214 Xiao, B., Pan, Y.M., Song, H., Song, W.L., Zhang, Y., and Chen, H.Y.
1215 (2021) Hydrothermal alteration processes of fluorapatite and implications for REE
1216 remobilization and mineralization. Contributions to Mineralogy and Petrology,
1217 176, 87.
1218 Xu, X.S., Dong, C.W., Li, W.X., and Zhou, X.M. (1999) Late Mesozoic intrusive
1219 complexes in the coastal area of Fujian, SE China: the significance of the
1220 gabbro-diorite-granite association. Lithos, 46, 299–315.
1221 Yang, Q., Xia, X.P., Cui, Z.X., Zhang W. F., Zhang, Y.Q., and Lai, C.K. (2021) SIMS
1222 simultaneous measurement of oxygen-hydrogen isotopes and water content for
1223 hydrous geological samples. Journal of Analytical Atomic Spectrometry, 36, 706–

715.

Zandomeni, P.S., Verdecchia, S.O., Baldo, E.G., Galindo, C., Moreno, J.A., Dahlquist, J. A., Casquet, C., Morales Camerà, M.M., Basei, M.A.S., and Ramacciotti, C.D. (2021) Early Ordovician magmatism in the Sierra de Ancajàn, Sierras Pampeanas (Argentina): implications for the early evolution of the proto-Andean margin of Gondwana. Journal of Iberian Geology, 47, 39–63.

Zeng, L.J., Bao, Z.W., Shan, Q., Yang, W.B., Zhao, Y., and Li, N.B. (2016a) Magmatic-hydrothermal evolution of highly fractionated granite: Evidence from the Kuiqi miarolite in Fujian province, China. Journal of Asian Earth Sciences, 123, 100–110.

Zeng, L.P., Zhao, X.F., Li, X.C., Hu, H., and McFarlane, C. (2016b) In situ elemental and isotopic analysis of fluorapatite from the Taocun magnetite-apatite deposit, Eastern China: Constraints on fluid metasomatism. American Mineralogist, 101, 2468–2483.

Zhang, B., Guo, F., Zhang, X.B., Wu. Y.M., Wang, G.Q., and Zhao, L. (2019). Early cretaceous subduction of Paleo-Pacific Ocean in the coastal region of SE China: Petrological and geochemical constraints from the mafic intrusions. Lithos, 334-335, 8–24.

Zhang, G.W., Guo, A.L., Wang, Y.J., Li, S.Z., Dong, Y.P., Liu, S.F., He, D.F., Cheng, S. Y., Lu, R.K., and Yao, A.P. (2013) Tectonics of South China continent and its implications. Science China Earth Sciences, 56, 1804–1828.

Zhang, X.B., Guo, F., Zhang, B., Zhao, L., Wu, Y.M., Wang, G.Q., and Alemayehu, M.

(2020) Magmatic evolution and post-crystallization hydrothermal activity in the early Cretaceous Pingtan intrusive complex, SE China: Records from apatite geochemistry. Contributions to Mineralogy and Petrology, 175, 35.

Zhang, X.B., Guo, F., Zhang, B., Zhao, L., and Wang, G. Q. (2021) Mixing of cogenetic magmas in the Cretaceous Zhangzhou calc-alkaline granite from SE China recorded by in-situ apatite geochemistry. American Mineralogist, 106, 1679–1689.

Zhang, Y.X. (1999) H_2O in rhyolitic glasses and melts: Measurement, speciation, solubility, and diffusion. Reviews of Geophysics, 37, 493–516.

Zhao, J.L., Qiu, J.S., Liu, L., and Wang, R.Q. (2016) The late cretaceous I- and A-type granite association of Southeast China: Implications for the origin and evolution of post-collisional extensional magmatism. Lithos, 240-243, 16–33.

Zhao, L., Guo, F., Zhang, X.B., and Wang, G.Q. (2021) Cretaceous crustal melting records of tectonic transition from subduction to slab rollback of the Paleo-Pacific Plate in SE China. Lithos, 384-385, 105985.

Zhao, Z.H., Wang, Z.G., Zou, T.R., and Zeng, T.Z.Z (1999) Study of petrogenesis of alkali-rich intrusive rock of Wulungu, Xinjiang. Geochimica, 3, 205–220 (In Chinese with English abstract).

Zhou, X.M., and Li, W.X. (2000) Origin of late Mesozoic igneous rocks in Southeastern China: implications for lithosphere subduction and underplating of mafic magmas. Tectonophysics, 326, 269–287.

Zhou, X.M., Sun, T., Shen, W.Z., Shu, L.S., and Niu, Y.L. (2006) Petrogenesis of

1268 Mesozoic granitoids and volcanic rocks in South China: a response to tectonic
1269 evolution. Episodes, 29, 26–33.
1270 Zhu, X.L., Yang, J.B., Hou, Q.Y., and Zhao, Z.D. (2021) Petrogenesis of Fuzhou
1271 composite pluton: Constraint from zircon U-Pb geochronology, geochemistry, and
1272 Hf isotopes. Acta Petrological Sinica, 37, 1235－1254(in Chinese with English
1273 abstract).
1274 Zirner, A.L.K., Marks, M.A.W., Wenzel, T., Jacob, D.E., and Markl, G. (2015) Rare
1275 earth elements in apatite as a monitor of magmatic and metasomatic processes:
1276 The Ilimaussaq complex, South Greenland. Lithos, 228–229, 12–22.
1277

Figure captions

Figure 1 Simplified geological maps showing the tectonic location (a, after Zheng et al., 2013), distribution of late Mesozoic granites and volcanic rocks in the coastal region of SE China (b, after Zhang et al., 2019), and Fuzhou I-A-type granitic complex (c, after Zeng et al. 2016a). Samples DY01–11 were collected in Danyang pluton, FZ08–09 and JX01–04 were collected in Fuzhou pluton, and KQ01–22 were collected in Kuiqi pluton.

Figure 2 Representative microphotos (a, c, e, g) and back-scattered electron (BSE) images (b, d, f, h) of the Fuzhou I-A-type granitic complex. Apatite is texturally hosted in rock-forming and accessory minerals such as plagioclase, hornblende, biotite and ilmenite. Mineral abbreviations: Pl – plagioclase; Kfs – K-feldspar; Hb – hornblende; Bt – biotite; Qtz – quartz; Arf – arfvedsonite; Ap – apatite; Ilm – ilmenite; Zr – zircon.

Figure 3 Total alkali vs. SiO_2 (a, TAS, after Middlemost 1994), A/CNK (molar ratio of $Al_2O_3/(CaO + Na_2O + K_2O)$ vs. A/NK (molar ratio of $Al_2O_3/(Na_2O + K_2O)$ (b), $FeO^T/(FeO^T+MgO)$ vs SiO_2 diagram(c, after Frost et al., 2001), 10000Ga/Al versus FeO^T/MgO (d, after Whalen et al., 1987), primitive mantle-normalized incompatible trace element spidergrams (e, f) and chondrite-normalized rare earth element (REE) patterns (g, h) for the Fuzhou I-A-type granitic complex. Normalization values for REEs and incompatible trace elements are from Sun and McDonough (1989) and

hereafter. The grey square represents the literature data of I-type granitoids, grey triangle represents the literature data of A-type granites, and the shaded fields denote the trace element variation ranges of literature data (Chen et al., 2013, 2019a, 2019b; Gao et al., 2018; Liu et al., 2012, 2013, 2018). Data sources are listed in Table S1.

Figure 4 Chemical mapping results of F, Cl, S, Na and Ce in apatite from I-type granite (a, 19FZ-08) and A-type granite (b, 21KQ-05). The red spot in Figure 4b denotes the occurrence of monazite.

Figure 5 F-Cl-OH ternary diagram for apatite from the Fuzhou I-type granitoids and A-type granites (a), with mole fractions calculated from the EPMA data in supplementary Table S2. F versus Cl concentrations of apatite, showing a broad negative correlation (b).

Figure 6 H_2O (ppm) versus δD (‰) plots of apatite from the I- type granitoids (a) and A-type granites (b), and apatite H_2O versus whole-rock zirconium saturation temperature (T_{Zr}) of Fuzhou I-A-type granitic complex (c).

Figure 7 Diagrams of apatite H_2O versus Cl (a), F (b), Ce (c), ∑REE (d), Sr/Y ratio (e) and La/Sm ratio (f) of the Fuzhou I-A-type granitic complex. See details in the text. Mineral abbreviations: Pl – plagioclase; Hb – hornblende; Ap – apatite.

1322 **Figure 8** A profile analysis of H_2O and H isotopes on a single apatite crystal, showing
1323 an increase of H_2O against a decrease of δD from the core to rims.
1324
1325 **Figure 9** Fractional crystallization modelling of the I-type granitoids (a, b, d) and
1326 peralkaline A-type granites (a, c, d) based on whole-rock elemental geochemistry. We
1327 assume a monzonite sample (19DY-07 has the lowest SiO_2) and a peralkaline granite
1328 (21KQ-02 have the highest Sr and H_2O contents) to represent the likely candidates of
1329 parent magma respectively for I-type granitoids and A-type granites. The involved
1330 partition coefficients (Kd) between mineral and melt are from the website:
1331 https://kdd.earthref.org/KdD and listed in Table 1 of Supplementary Materials.
1332
1333
1334 **Figure 10** A microphoto (a) and BSE image (b) of arfvedsonite and aegirine and a
1335 profile compositional analysis (c), showing the increase of Na_2O, FeO, Zr and Hf
1336 contents from the arfvedsonite to aegirine.
1337
1338 **Figure 11** A diagram of F versus ∑REE of apatite from the Fuzhou I-A-type granitic
1339 complex. Shaded fields represent the literature data, including apatite in alkaline
1340 igneous rocks (Mao et al., 2016; Zirner et al., 2015 and references therein) and apatite
1341 in I-type granitoids (Belousova et al., 2001; Chu et al., 2009; Sha and Chappell, 1991;
1342 Tollari et al., 2008; Sun et al., 2021; Zhang et al., 2020, 2021).
1343

1344 **Figure 12** Numerical modelling of devolatilization process in the I-type granitoids (a)
1345 and A-type granite (b). The δD variation during degassing is respectively calculated
1346 by Eq. 1 (open system) and Eq. 2 (closed system), *f* is the proportion of residual water
1347 in the melt, α is the fractionation factor of H isotopes. The initial conditions include
1348 H_2O = 1869 ppm and δD = −190 ‰, H_2O =1223 and δD = −196‰ from the apatite
1349 grain in a monzogranite and A-type alkaline granites, respectively. Solid lines denote
1350 the closed-system degassing and the dotted lines illustrate the open-system degassing.
1351 See details in the text.
1352
1353 **Figure 13** Diagrams of H_2O (ppm) versus H_2O/Ce ratio (a) and F/Cl ratio (b) of
1354 apatite. Following the decrease of H_2O, the rapid decrease of H_2O/Ce coupled with
1355 abrupt increase of F/Cl indicate the significant role of magmatic degassing in the
1356 late-stage evolution of both I- and A-type granitoids.
1357
1358 **Figure 14** A schematic cartoon illustrating the magmatic evolution and degassing
1359 processes of the Fuzhou A-I-type granitic complex. Rollback of the subducted
1360 paleo-Pacific slab and the resultant asthenospheric upwelling triggered the melting of
1361 the recently accreted arc crust to form the primary magma represented by monzonite
1362 (Zhou et al., 2006; Guo et al., 2021). The following magmatic differentiation, fluid
1363 metasomatism and degassing to varying degrees produced the geochemical variations
1364 from the I-type to peralkaline A-type granitoids. See details in the text.
1365

Figure 1

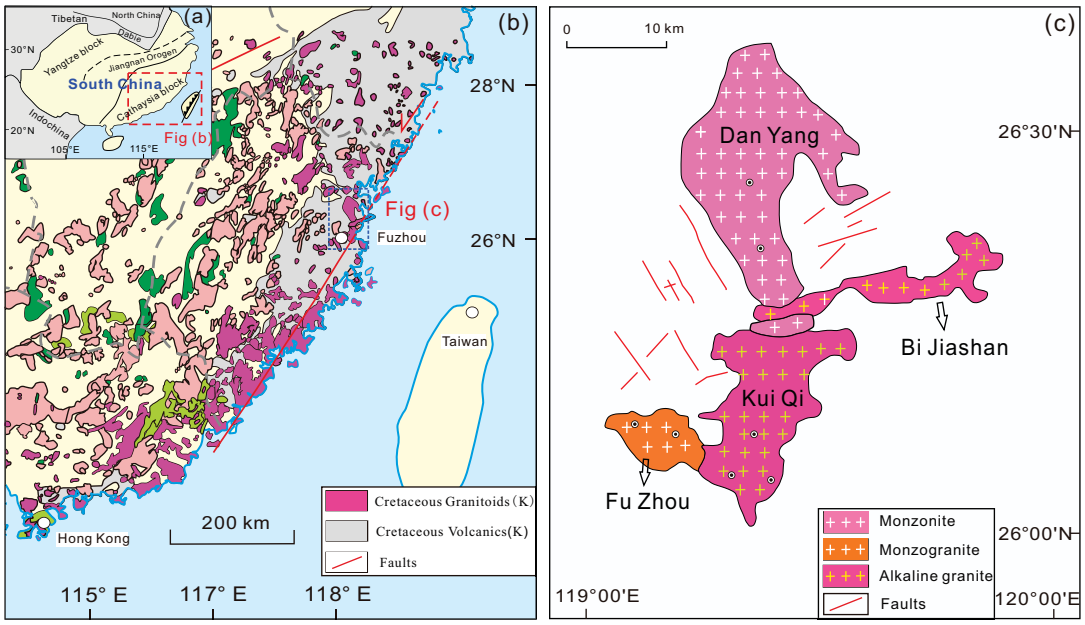

Figure 2

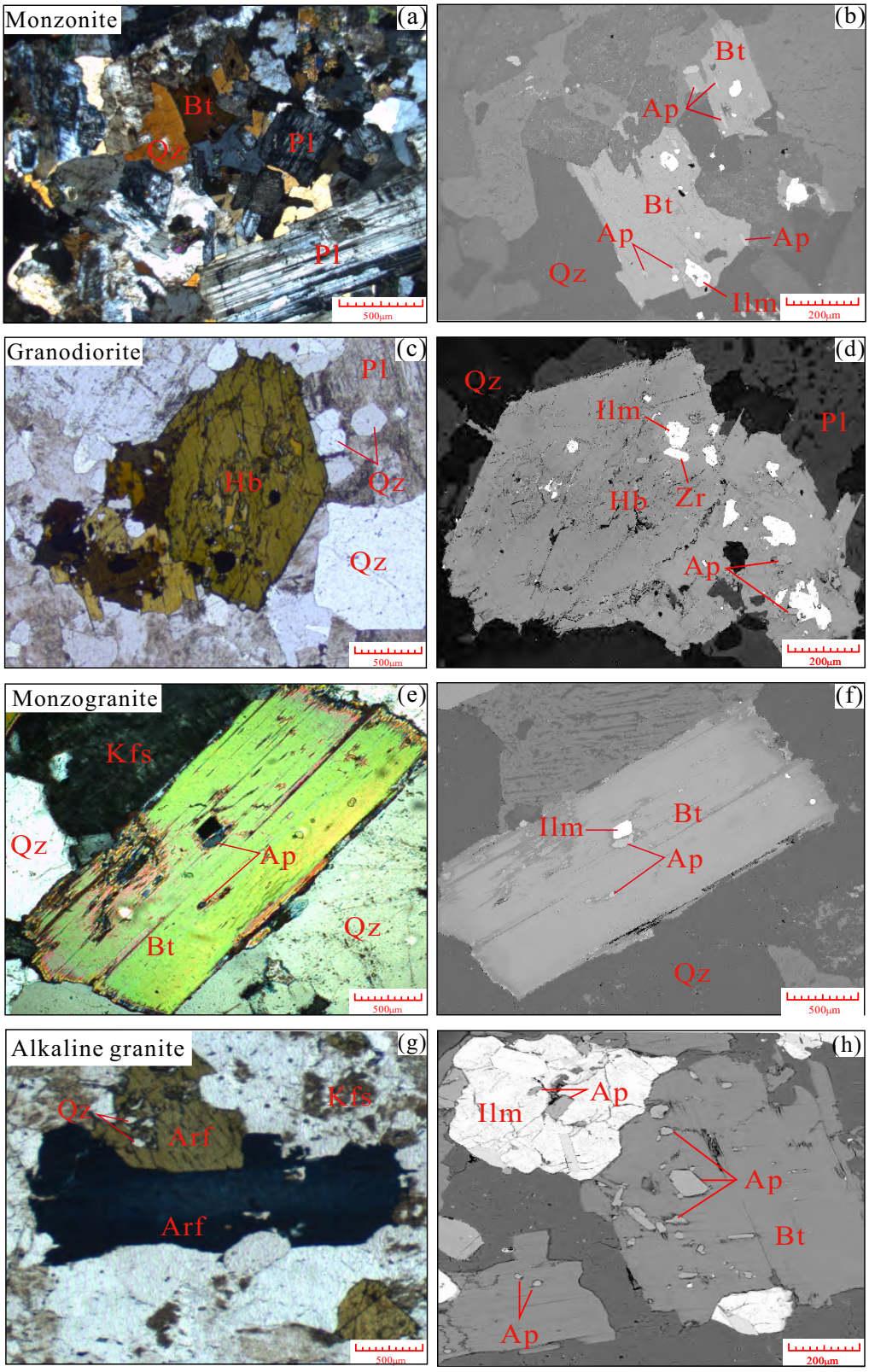

This is the peer-reviewed, final accepted version for American Mineralogist, published by the Mineralogical Society of America.
The published version is subject to change. Cite as Authors (Year) Title. American Mineralogist, in press.
DOI: https://doi.org/10.2138/am-2023-8936. http://www.minsocam.org/

Figure 3

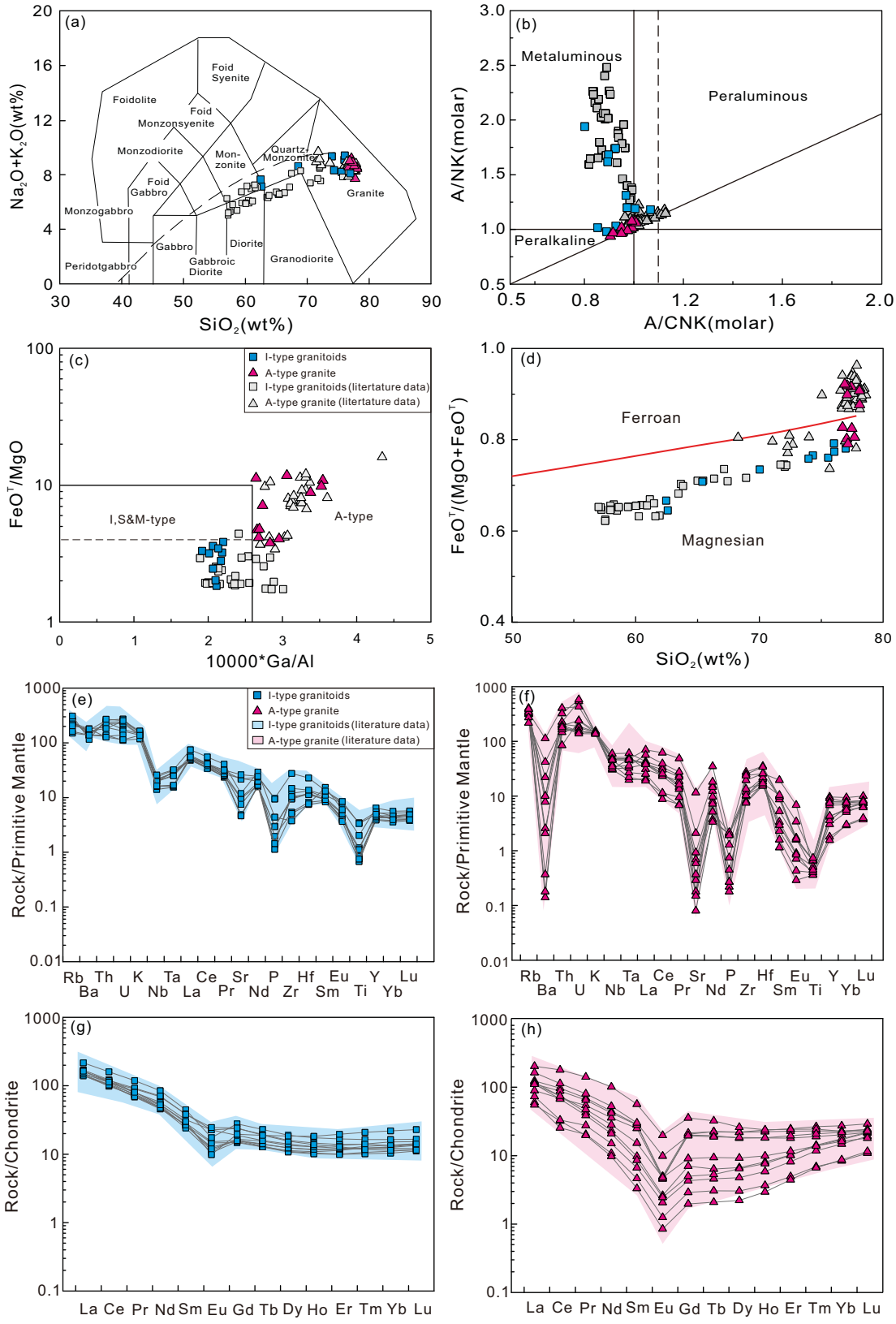

Figure 4

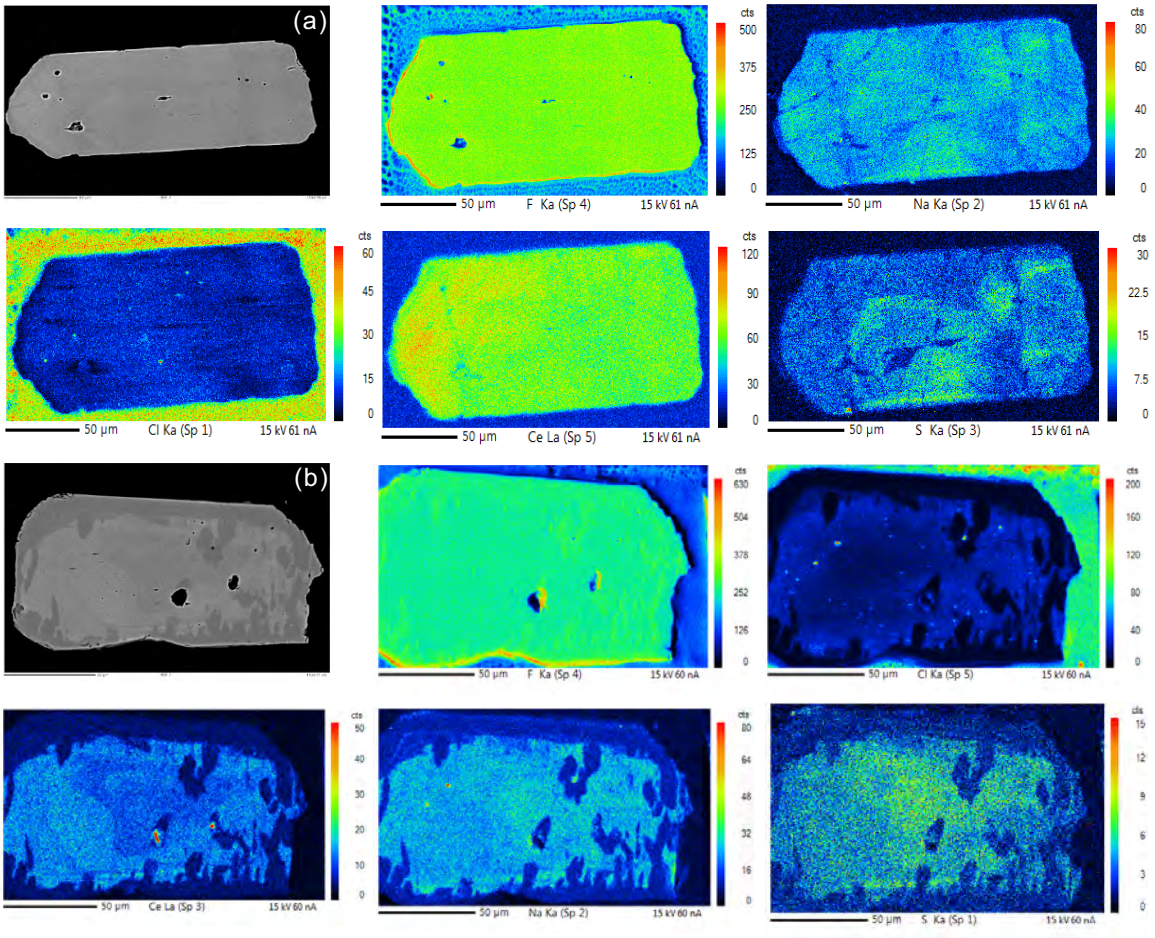

Figure 5

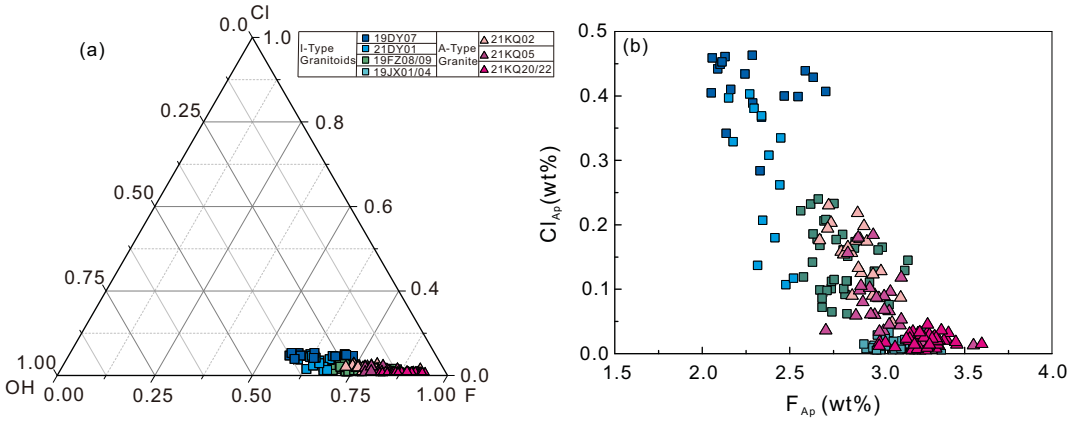

This is the peer-reviewed, final accepted version for American Mineralogist, published by the Mineralogical Society of America.
The published version is subject to change. Cite as Authors (Year) Title. American Mineralogist, in press.
DOI: https://doi.org/10.2138/am-2023-8936. http://www.minsocam.org/

Figure 6

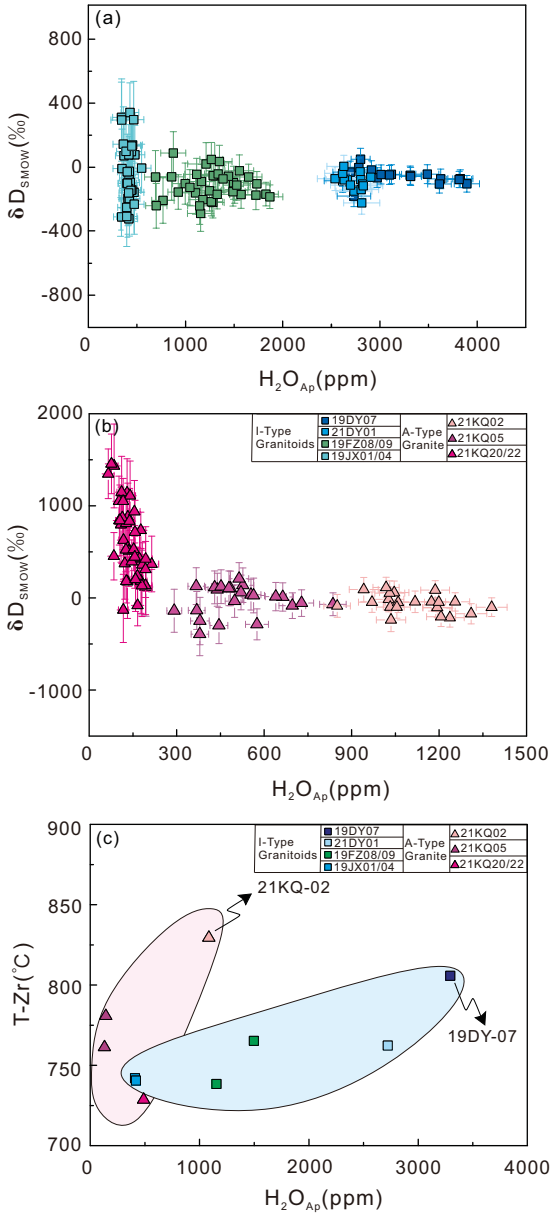

Figure 7

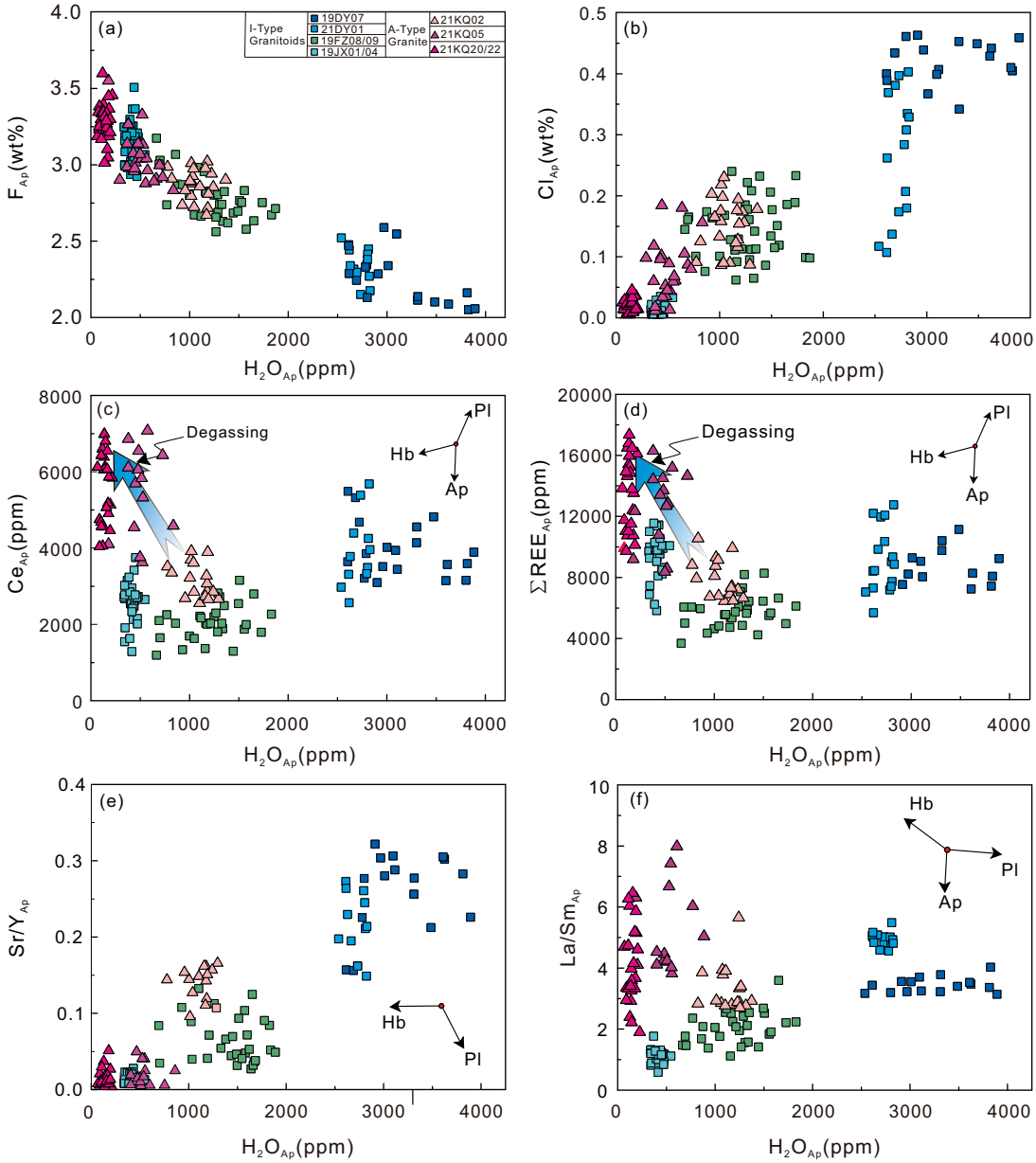

Figure 8

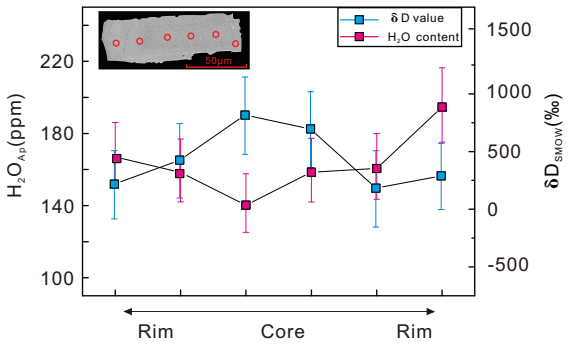

This is the peer-reviewed, final accepted version for American Mineralogist, published by the Mineralogical Society of America.
The published version is subject to change. Cite as Authors (Year) Title. American Mineralogist, in press.
DOI: https://doi.org/10.2138/am-2023-8936. http://www.minsocam.org/

Figure 9

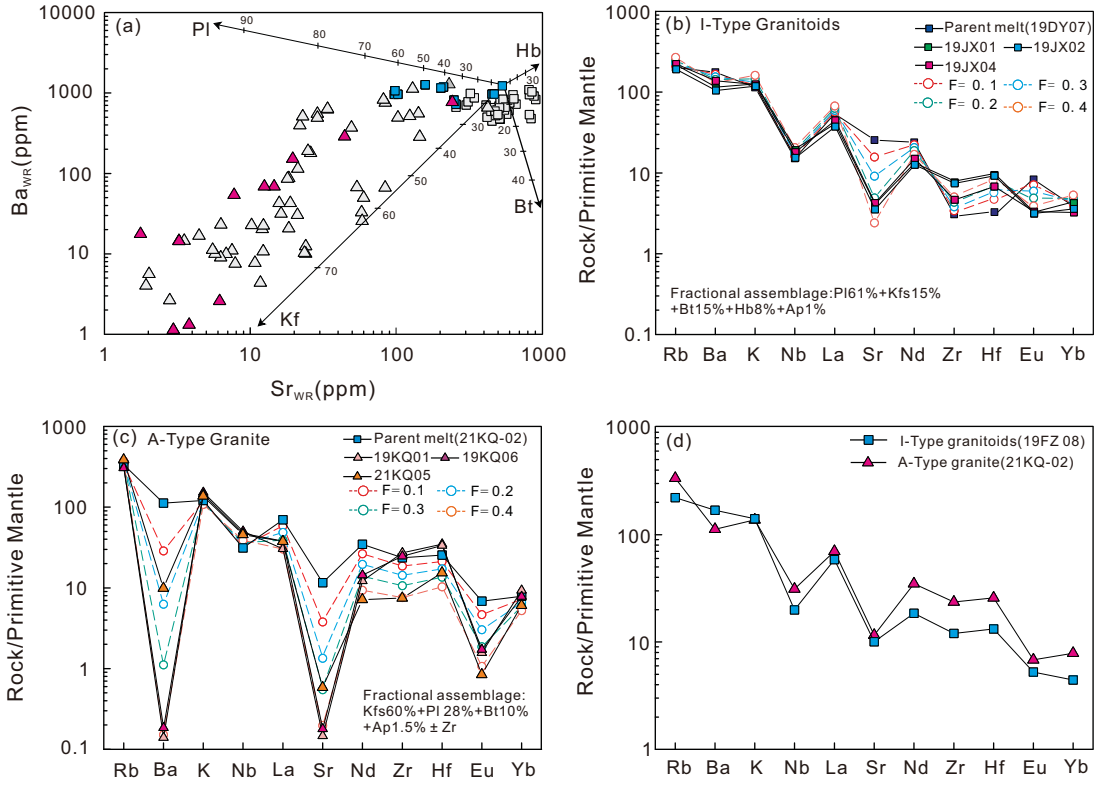

Figure10

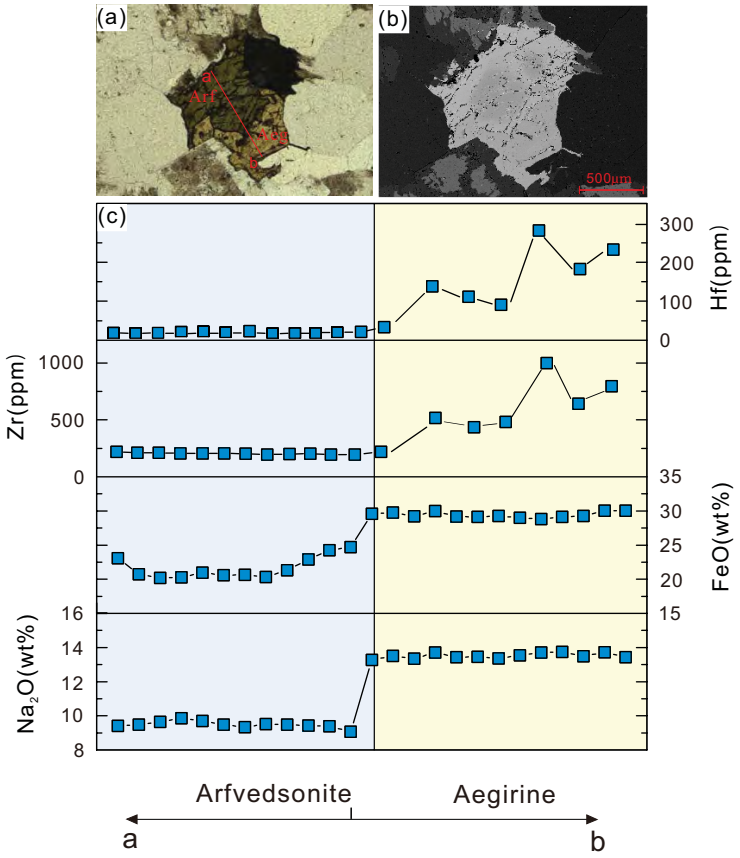

Figure 11

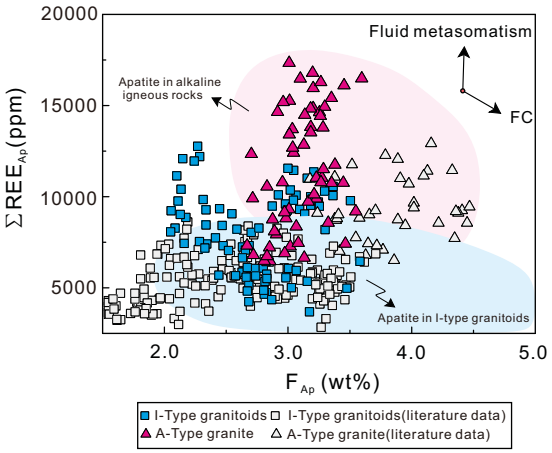

Figure 12

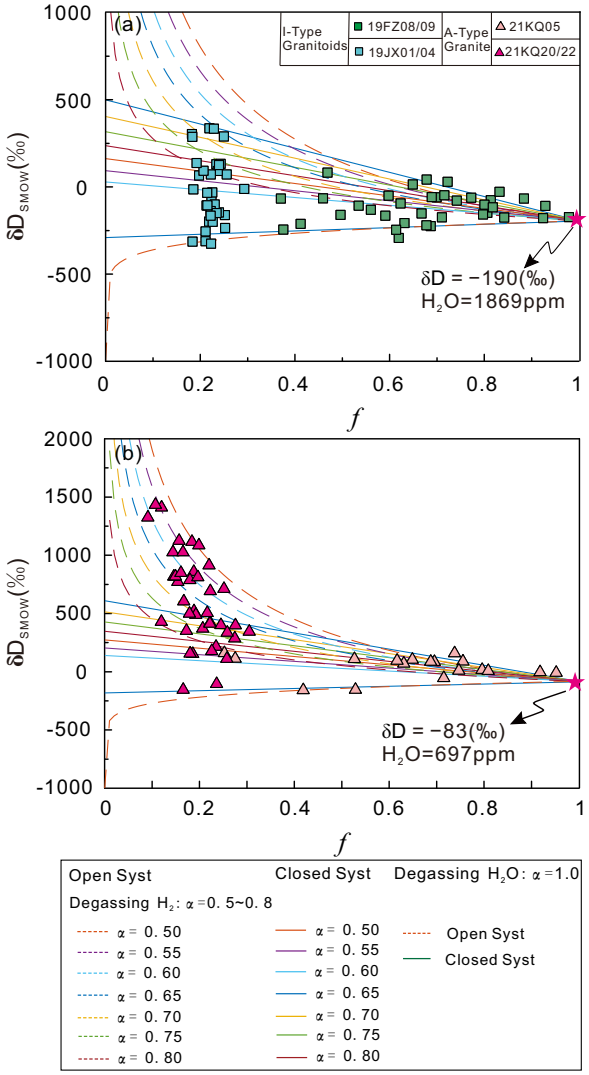

Figure 13

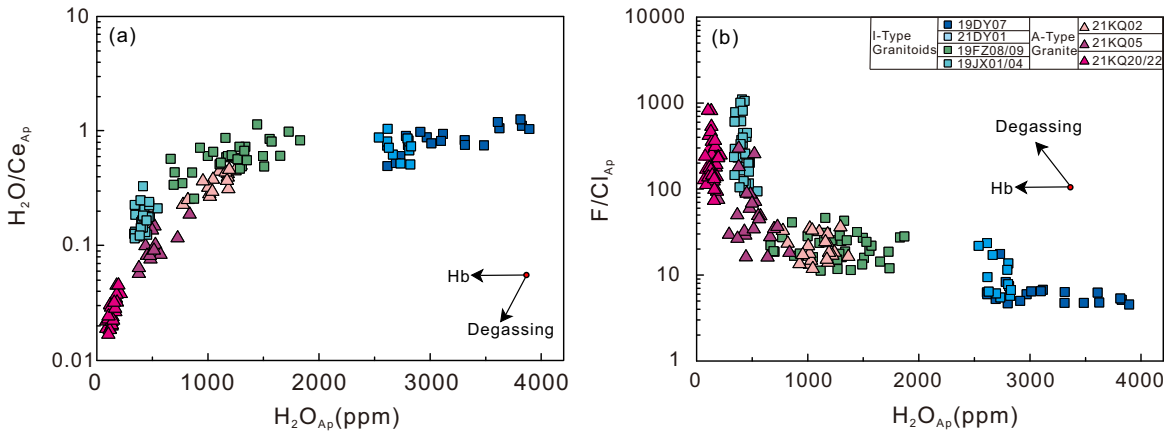

Figure 14